CORRELATION OF NSWC GROUNDING TESTS WITH MIT THEORY

by

Iñigo Javier Puente

B.S. Ocean Engineering
Massachusetts Institute of Technology
(1994)

Submitted to the Department of Ocean Engineering
in Partial Fulfillment of the Requirements
for the Degree of

MASTER OF SCIENCE
In Ocean Engineering
at the

MASSACHUSETTS INSTITUTE OF TECHNOLOGY
May 1995

© Iñigo Javier Puente 1995. All rights reserved.

The author hereby grants to MIT permission to reproduce and to distribute publicly paper and electronic copies of this thesis document in whole or in part.

Signature of Author_____
Department of Ocean Engineering
May 1995

Certified by_____
Tomasz Wierzbicki, Professor of Applied Mechanics
Thesis Supervisor

Accepted by_____
A. Douglas Carmichael, Chairman Department Graduate Committee
Department of Ocean Engineering

MASSACHUSETTS INSTITUTE
OF TECHNOLOGY

JUL 28 1995

Barker Eng

LIBRARIES

CORRELATION OF NSWC GROUNDING TESTS WITH MIT THEORY

by

Iñigo Javier Puente

Submitted to the Department of Ocean Engineering on May 17, 1995, in partial fulfillment of the requirements for the degree to Master of Science in Ocean Engineering.

ABSTRACT

Over the last three years, the Joint MIT-Industry Program on Tanker Safety has conducted extensive research on the subject of ship grounding and collision accidents. In a previous Tanker Safety Report [2], the NSWC large scale grounding experimental results were used to validate the existing Minorsky/Vaughn theory. The correlation was shown to leave room for improvement. In this thesis, a complete new theoretical approach to the problem of ship grounding is developed. This new approach is based on the concept of Superelements that was first introduced in the automotive industry. The underlying principle of the new theory is to investigate the separate contributions of the large structural elements identified in the model, and then to assemble those contributions into the total response of the structure. In this thesis, it will be shown that the correlation of the new MIT theory with NSWC large scale grounding experimental results constitutes a significant improvement on the existing Minorsky/Vaughn theory.

Thesis Supervisor: Tomasz Wierzbicki
Title: Professor of Applied Mechanics

Acknowledgment

First and foremost, I would like to thank my advisor Professor Tomasz Wierzbicki for his guidance and help in completing this thesis. I would also like to thank the research team of the Joint MIT-Industry Program on Tanker Safety, including Dr. Sung K. Choi of Deawoo, Dan Pippenger of MIT, and Bo Simonsen of the Technical University of Denmark, for their contributions to the development of the new ship grounding theory. Many thanks are due to Teresa Coates for her invaluable help in dealing with administrative matters.

I wish to extend my gratitude to all the people that over my five years at MIT have impressed upon me the desire of learning which has culminated in this masters thesis.

Finally, I would like to offer a special recognition for my mother Agurtzane, my family, and my friends, for their love and support, without which any enterprise would lose its meaning. To them I dedicate this thesis.

Light, Love, Destiny.

Table of Contents

List of Figures....(7)

List of Tables....(8)

List of Symbols....(9)

Chapter 1. Introduction....(10)

Chapter 2. Description of NWSC Grounding Experiment....(13)

2.1 Description of the Experimental Apparatus....(13)

2.2 Description of the Double-Hull Ship Bottom Model....(14)

2.3 Analysis of the Experimental Results....(14)

2.3.1 Experimental Results....(14)

2.3.2 Energy Balance....(15)

2.3.3 Observations on Hull Failure Modes....(17)

Chapter 3. Contribution of Outer Plate to the Total Resisting Force....(23)

3.1 Introduction....(23)

3.2 Outer Plate Cutting Initiation....(24)

3.2.1 Outer Plate Cutting Initiation Governing Equation....(24)

3.2.2 Outer Plate Cutting Initiation Boundaries....(25)

3.3 Outer Plate Steady State Cutting....(26)

3.3.1 Derivation of Outer Plate Steady State Cutting Force....(26)

3.3.1.1 Curved Flaps Model Kinematics....(26)

3.3.1.2 Energy Dissipation....(26)

3.3.1.3 Bending Energy Rate....(28)

3.3.1.4 Near-Tip Zone Membrane Energy Rate....(30)

3.3.1.5 Membrane Energy Rate in the Transition Zones....(32)

3.3.1.6 Theoretical Outer Plate Steady State Cutting Force without Friction....(33)

3.3.1.7 Geometric Relation between R and B for a Conical Wedge....(34)

3.3.1.8 Closed Form Solution for the Outer Plate Steady State Cutting Force....(34)

3.3.1.9 Friction Contribution to the Outer Plate Steady State Cutting Force....(35)
3.3.2 Geometry of Outer Plate Steady State Cutting....(36)
3.3.3 Outer Plate Steady State Cutting Boundaries....(38)
3.4 Summary of Outer Plate Contribution to the Total Resisting Force....(39)
Chapter 4. Contribution of Inner Plate to the Total Resisting Force....(47)
4.1 Introduction....(47)
4.2 Inner Plate Cutting Initiation....(48)
4.2.1 Inner Plate Cutting Initiation Governing Equation....(48)
4.2.2 Geometry of Inner Plate Cutting Initiation....(49)
4.2.3 Inner Plate Cutting Initiation Boundaries....(50)
4.3 Inner Plate Steady State Cutting....(51)
4.3.1 Derivation of Inner Plate Steady State Cutting Force....(51)
4.3.1.1 Straight Flaps Model Kinematics....(51)
4.3.1.2 Energy Dissipation....(51)
4.3.1.3 Friction Contribution to the Inner Plate Steady State Cutting Force....(53)
4.3.1.4 Closed Form Solution for the Inner Plate Steady State Cutting Force....(53)
4.3.2 Geometry of Inner Plate Steady State Cutting....(54)
4.3.3 Inner Plate Steady State Cutting Boundaries....(54)
4.4 Summary of Inner Plate Contribution to the Total Resisting Force....(54)
Chapter 5. Contribution of Transverse Frames to the Total Resisting Force....(61)
5.1 Introduction....(61)
5.2 Transverse Frame Cutting Force Governing Equation....(62)
5.3 Transverse Frame Contribution Boundaries....(63)
5.4 Summary of Transverse Frame Contribution to the Total Resisting Force....(64)
Chapter 6. Contribution of Longitudinal Girders to the Total Resisting Force....(70)
6.1 Introduction....(70)
6.2 Derivation of Longitudinal Girder Crushing Force....(70)

6.2.1 Model Kinematics.....(70)
6.2.2 Energy Dissipation.....(71)
6.2.3 Friction Contribution to the Longitudinal Girder Crushing Force.....(72)
6.2.4 Closed Form Solution for the Longitudinal Girder Crushing Force.....(72)
6.3 Longitudinal Girder Contribution Boundaries.....(73)
6.4 Summary of Longitudinal Girder Contribution to the Total Resisting Force.....(74)
Chapter 7. Conclusion.....(79)
7.1 Comparison of MIT Theory with NSWC Grounding Test.....(79)
7.2 Recommendations for Future Work.....(81)
7.3 Final Remarks.....(82)
References.....(84)
Appendix.....(86)
A1. Table of Numerical Values.....(77)
A2. Matlab Source Code.....(77)

List of Figures

Figure 2.1. Schematic View of NSWC Experimental Apparatus.....(18)
Figure 2.2. NSWC Grounding Test T-5 Model Geometry.....(19)
Figure 2.3. NSWC Grounding Test Velocity Data.....(20)
Figure 2.4. NSWC Grounding Test Rock Reaction Forces.....(21)
Figure 2.5. Global Coordinate System for Hull-Cone Interaction.....(22)
Figure 3.1. Aerial View of Cone Cutting through Outer Plate.....(40)
Figure 3.2. Outer Plate Initiation Force vs. Split Angle.....(41)
Figure 3.3. Curved Flaps Model Geometry.....(42)
Figure 3.4. Local Coordinate System for Curved Flaps Model.....(43)
Figure 3.5. Side View of Cone-Outer Plate Interaction.....(44)
Figure 3.6. Outer Plate Steady State Force vs. Split Angle.....(45)
Figure 3.7. Theoretical Contribution of Outer Plate to the Total Resisting Force.....(46)
Figure 4.1. Inner Plate Cutting Initiation Geometry.....(56)
Figure 4.2. Straight Flaps Model Geometry.....(57)
Figure 4.3. Side View of Cone-Inner Plate Interaction.....(58)
Figure 4.4. Inner Plate Steady State Force vs. Split Angle.....(59)
Figure 4.5. Theoretical Inner Plate Contribution to the Total Resisting Force.....(60)
Figure 5.1. Transverse Frame Geometry.....(66)
Figure 5.2. Diamond Shape Geometry in Transverse Frame Cutting.....(67)
Figure 5.3. Phases of Transverse Frame Cutting.....(68)
Figure 5.4. Theoretical Transverse Frame Contribution to the Total Resisting Force.....(69)
Figure 6.1. Longitudinal Girder Deformation Geometry.....(75)
Figure 6.2. Side View of Longitudinal Girder Deformation Geometry.....(76)
Figure 6.3. Longitudinal Girder Force vs. Split Angle.....(77)
Figure 6.4 Theoretical Longitudinal Girder Contribution to the Total Resisting Force.....(78)
Figure 7.1. Comparison of MIT Theory with NSWC Experimental Results.....(83)

List of Tables

Table 2.1. Summary of NSWC Experiment Global Parameters.....(15)

Table 3.1. Summary of Outer Plate Contribution to the Total Resisting Force.....(39)

Table 4.1. Summary of Inner Plate Contribution to the Total Resisting Force.....(55)

Table 5.1. Summary of Transverse Frame Contribution to the Total Resisting Force.....(65)

Table 6.1. Summary of Longitudinal Girder Contribution to the Total Resisting Force...(73)

List of Symbols

θ	Plate split angle.
ϕ	Cone apex angle measured from the vertical.
σ_0	Material flow stress.
t	Plate thickness for all structural members.
μ	Coefficient of friction.
α	Angle of attack of structural assembly with respect to the ground.
c_1	Transverse frame spacing.
c_2	Perpendicular distance from outer plate leading edge to the first transverse frame.
R	Stable flap rolling radius.
V	Forward horizontal velocity of the structure with respect to the cone.
B	Curved flap induced conical wedge shoulder.
h	Vertical distance from cone vertex to the undeformed outer plate.
Δ	Height of the 90 degree cone.
Δ_1	Height of the conical rock.
r	Radius of the conical rock rounded tip dome.
l	Overall length of model assembly.
β	Rotation of the straight flap with respect to the undeformed inner plate.
δ	Vertical penetration of the conical rock into the inner plate.
d	Double hull height.
e	Perpendicular distance between top of spherical rock and outer plate leading edge.
x,y	Global coordinate system.
ξ,η	Local coordinate system.

Chapter 1

Introduction

1.1 Introduction

Over the last two years three large-scale oil tanker grounding experiments have been conducted by the Carderock Division of the Naval Surface Warfare Center (NSWC). An additional eight tests are being planned in the near future. At the time of this writing only results from the first grounding experiment were published in the open literature, Rodd [1]. This experiment represents a typical section of a conventional double hull tanker bottom structure with longitudinal and transverse framing. The T-5 Panel Buck geometry and scantlings were used for the one-fifth scale Grounding Model #1. The Grounding Model #1 is considered to be the baseline for subsequent, more elaborated double hull structural designs, and, therefore, the most general and representative case.

The objective of this thesis is to predict the total resisting force of the structure in the event of grounding against a conical rock and compare it with NSWC test results. In an earlier effort by Choi et al. [2], the grounding force developed in NSWC Model #1 was determined using the Minorsky/Vaughn method. The validity, in large scale experiments, of the Minorsky/Vaughan empirical formula, [13], [14], [15] and [16], for the prediction of the energy absorbed by a ship hull structure during collision and grounding accidents, has been challenged by Choi's correlation between the Minorsky approach and the NSWC Grounding Tests results, Choi et al. [2]. Choi found that this correlation was not satisfactory, both in terms of the magnitude of the grounding force and the total energy dissipated. The deficiencies in the Minorsky/Vaughan method can be attributed to three factors:

1. The inherent difficulty of defining the amount of *damaged* material around the rock, or other underwater obstacles.

2. The independence of Minorsky's empirical formula on the magnitude of the material yield stress, and hence its inability to distinguish amongst different types of materials, e.g. mild steel versus high strength steel.

3. The difficulty of determining the displaced volume of ship hull material and the area of tearing fracture for complex ship hull geometry, such as in the case of NSWC Grounding Tests.

In the present report, an alternative method of predicting grounding forces is introduced, based on the concepts of Superfolding and Supertearing elements. The Superelement approach to grounding calculations was developed for the Joint MIT-Industry Program on Tanker Safety and is documented in a number of technical reports. Each of these reports addressed particular failure modes of single structural elements. Examples of failure modes considered so far are concertina tearing of hull plating [9], central separation (also known as clean cut) [4], crushing of webs [10] and [11], and cutting of transverse frames and bulkheads [12]. Good correlation with small, intermediate and full scale tests was obtained at the level of individual structural elements.

A section of a double hull tanker represents a complex structural system. The NSWC intermediate scale test provides a perfect opportunity to validate the MIT theory in a realistic grounding configuration. However, the conical rock geometry and the relative position of the rock with respect to the double hull used in the NSWC test have introduced a number of failure modes that had not been considered in the existing reports of the Tanker Safety Program. In an attempt to improve the analytical techniques for predicting damage to ships in collision and grounding accidents, the Joint MIT-Industry Program on Tanker Safety was commissioned by NSWC to conduct additional research and develop new theoretical models for the prediction of damage. The correlation of the new MIT theory with NSWC Grounding Tests results has turned out to be an improvement over the existing Minorsky/Vaughan method.

The spirit of the MIT theory is to investigate the individual contributions of all structural members present in the double hull ship structural configuration of NSWC Grounding Tests, and to account for the effect of the material yield stress in all calculations.

In this document, theoretical models are developed for the energy dissipation modes of each contributing structural member and, in the end, the individual contributions are assembled and compared with the results of the NSWC Grounding Tests.

All calculations were conducted using Matlab software. A hard copy of the input file is included in the Appendix.

Chapter 2

Description of NSWC Grounding Experiment

2.1 Description of the Experimental Apparatus

In NSWC tests, the Grounding Test Machine developed by HI-TEST Laboratories, Inc., in Arvonia, Virginia, is employed. The Grounding Test Machine enables researchers to simulate grounding conditions for Oil Tanker in the 30,000 to 40,000 ton category, at one-fifth scale. Figure 2.1 shows a schematic view of the experimental apparatus.

The test vehicle, weighing 223 tons, consists of a floating shock platform (FSP) mounted onto two railroad cars. The one-fifth scale ship double-hull bottom model is mounted onto the underside of the test vehicle. The whole assembly is constrained from vertical motion by a system of outriggers, so as to prevent the occurrence of derailment. In addition, some 260,000 pounds of ballast, in the form of concrete blocks, are loaded onto the test vehicle, so that its total weight amounts to 500,000 pounds.

The entire test assembly sits on top of an incline slope. At the required time, the test vehicle is released and let to accelerate freely under the force of its own weight, down the incline ramp. At the bottom of the ramp, the test vehicle engages with a cone shaped rock, mounted onto a 2.6 million pound reaction mass and containing the instrumental apparatus, at a speed of 12 knots, or 20 ft/sec. The rock itself is a 90 degree cone, 36 inches high and with a 7 inch radius spherical dome, made up of laminated steel plates and weighing approximately 13,000 pounds. The entire collision process is recorded by high speed 16mm cameras, video cameras, and various other recording devices.

2.2 Description of the Double-Hull Ship Bottom Model

The structural model employed in NSWC Grounding Tests represents a conventional T-5 double hull oil tanker bottom with transverse and longitudinal framing. The model geometry is shown in figure 2.2, which includes the double hull bottom arrangement, the forward and aft transverse bulkheads, and heavy sideplates representing the stiff center line longitudinal bulkhead and bilge of the ship .

The model is installed such that it is inclined by a 7.4 degree angle with respect to the horizontal. The purpose of the angle of attack is to delay the engagement of the rock with the inner plate, so as to be able to observe the actual initiation of rupture of the inner shell. Thus, the rock tip enters the model structure at the leading edge just below the inner bottom, and exists at the trailing edge high enough to ensure rupture of the inner shell. This exiting height of the cone was arbitrarily defined as twice the double-hull height.

The model structure was manufactured from ASTM A569 steel plating, with measured yield and ultimate stresses of 41 ksi and 50 ksi, respectively.

2.3 Analysis of the Experimental Results

2.3.1 Experimental Results

In addition to visual evidence of the failure mechanisms provided by the image recording devices, the instrumental set up produced data of the time history of the model velocity, and of the reaction forces measured by load cells located on the rock. These results are plotted and reproduced in figures 2.3 and 2.4, where velocity and forces are plotted with respect to the traveling distance of the model, relative to the cone. A summary of the principal global parameters measured in the experiment is given in table 1.1, where all quantities were measured with respect to the inertial (fixed) reference frame (x,y) with the origin at the base of the cone, as shown in figure 2.5.

$M = 0.5 \cdot 10^6\ lbs$	total weight of the test sled with hull section attached
$M_r = 2.6 \cdot 10^6\ lbs$	weight of the concrete reaction mass
$V_0 = 20.1 \quad ft/\text{sec}$	initial velocity of the sled
$V_f = 12.1 \quad ft/\text{sec}$	final velocity of the sled
$F_H(x) \quad [lbs]$	hull resisting force in the horizontal direction
$F_V(x) \quad [lbs]$	hull resisting force in the vertical direction

Table 2.1: Summary of NSWC Experiment Global Parameters

In this section, a global analysis of the above experimental data will be performed with the intention of checking the internal consistency of the results and learning about the nature of the contact forces between the hull and the conical rock. In addition. some observations will be made on the failure mechanics of the main structural components of the hull. Based on these observations, theoretical models will be developed in subsequent chapters to predict the hull grounding resisting force.

2.3.2 Energy Balance

Because of the fact that the sled is constrained from vertical motion, as described in section 2.2, the loss of kinetic energy ΔE_k must be equal to the total external work done on the system, that is

$$\Delta E_k = W \tag{1.1}$$

The kinetic energy loss in equation (1.1) can easily be calculated using the test data from table 1.1. Hence

$$\Delta E_k = \frac{1}{2} M\left(V_0^2 - V_f^2\right) = 2.0 \cdot 10^6 \quad [lbs \cdot ft] \tag{1.2}$$

The total external work done on the Sled-Hull Model system goes into plastic distortion, fracture and friction components. The aggregate sum of these components is measured by load cells positioned at the base of the conical rock. By definition the incremental work is

$$dW = F_H \, dx + F_V \, dy \tag{1.3}$$

where x and y are the directions of the coordinate axes in figure 2.5. However, because of the constraint on vertical motion, $dy = 0$. Therefore, only the horizontal force contributed to the work done. The substantial vertical force developed in the experiment should be considered as a reaction force. Note that in a real ship, the vertical force on the hull will produce pitching and rolling motion of the hull. The total energy dissipated by the hull becomes

$$W = \int_0^{x_f} F_H(x) \, dx \tag{1.4}$$

where x_f is the total distance traveled by the hull when in contact with the cone. Numerical integration of the experimentally measured horizontal hull resisting force, shown in figure 2.4, gives

$$W = 2{,}098{,}800 \quad [lbs \cdot ft] \tag{1.5}$$

The ratio of the kinetic energy loss to the total work is calculated from equations (1.2) and (1.5) as

$$\frac{\Delta E_k}{W} = 0.953 \tag{1.6}$$

The energy unaccounted for in the measurements is 4.7 % of the total energy input. This is an acceptable error considering the size of the experiment and the difficulties in handling such large systems. Possible sources of discrepancies could arise from inaccurate estimation of the mass of the sled, measurement of velocities and small systematic errors in the force acquisition system.

2.3.3 Observations on Hull Failure Modes

From the photographs of the damaged hull shown in the experimental paper by Rodd [1] and a video of the test produced by NSWC, several observations concerning failure patterns of the structural elements can be made. These observations will then be used in the next chapters to develop realistic deformation models of the hull. Thus,

1. The torn and displaced outer shell conformed to the shape of the conical rock. This observation is used in developing a computational model of the plate cutting by a conical wedge (see Chapter 3).
2. The inner shell wrapped around the tip of the rock, but was also displaced all the way to the longitudinal girders. The implications of the above deformation pattern are discussed in Chapter 4.
3. No weldment failures are visible.
4. Insufficient lateral support of the model resulted in the overall contraction of the section of the hull over the last two transverse frames. The above effect of the free boundary should be much weaker for double length models to be tested in the future.
5. More information on the damage pattern of the transverse and longitudinal frames could be retrieved had the hull been cut into pieces to expose the hidden members. Therefore, the assumptions regarding failure modes of these members should be regarded as tentative. These assumptions will be revised as new experimental data become available.

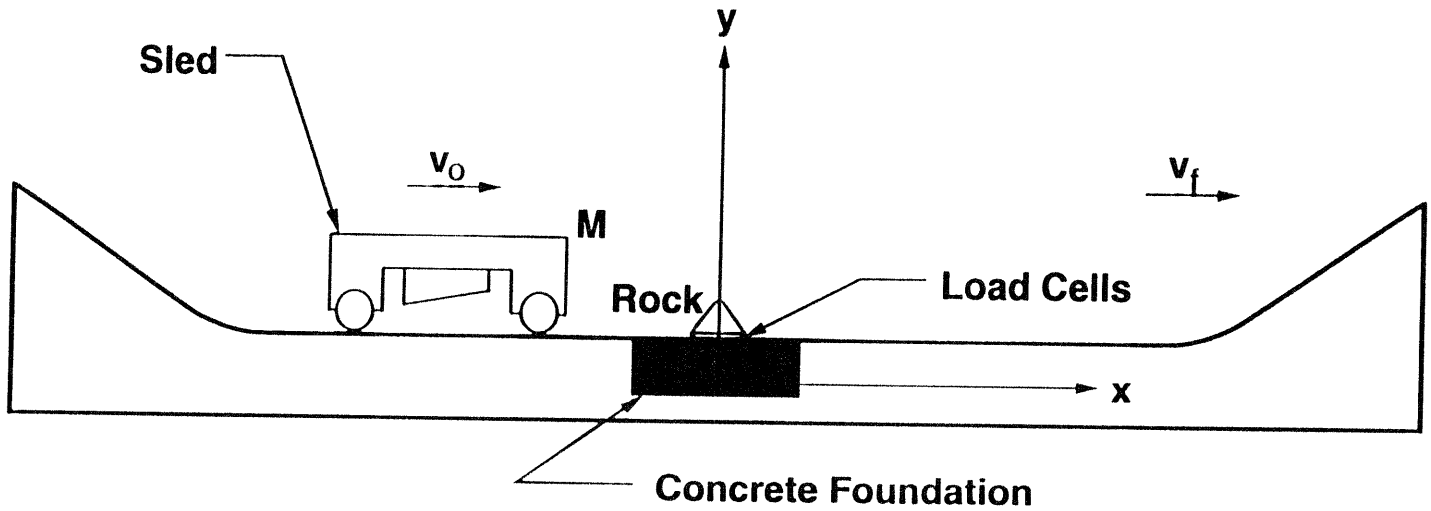

Figure 2.1. Schematic View of NSWC Experimental Apparatus

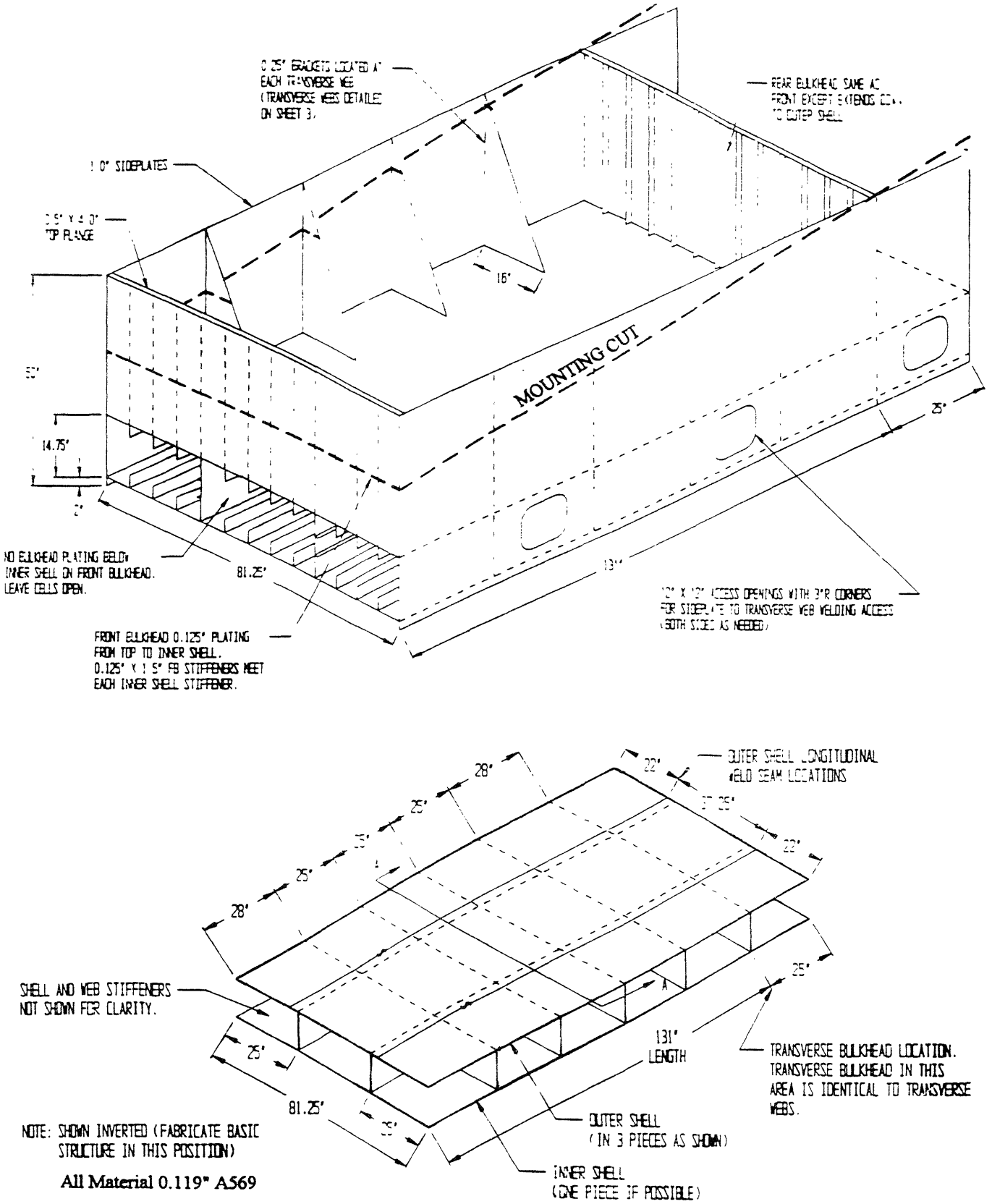

Figure 2.2. NSWC Grounding Test T-5 Model Geometry

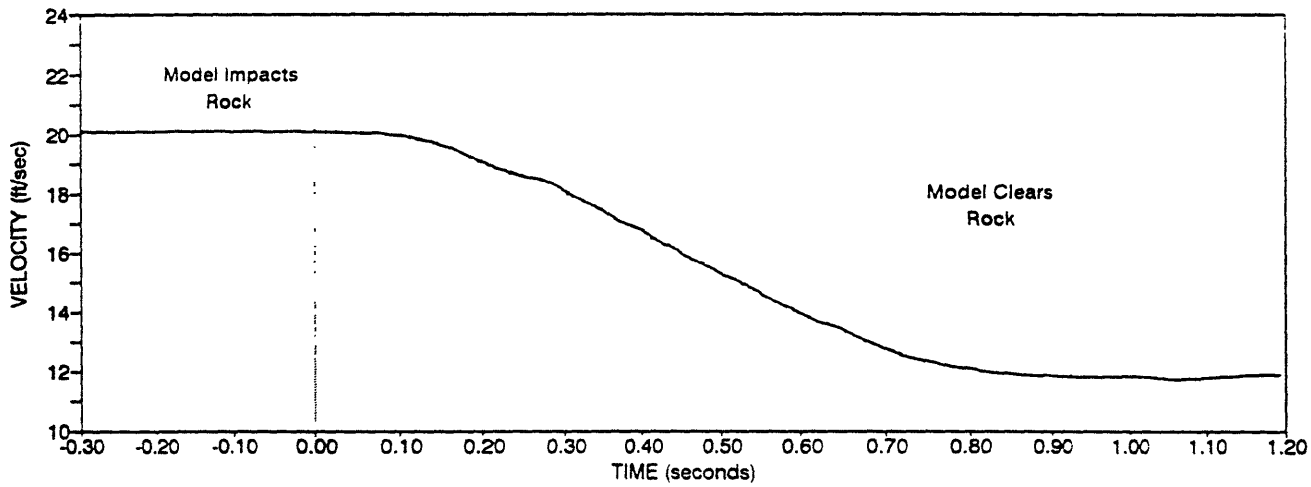

Figure 2.3. NSWC Grounding Test Velocity Data

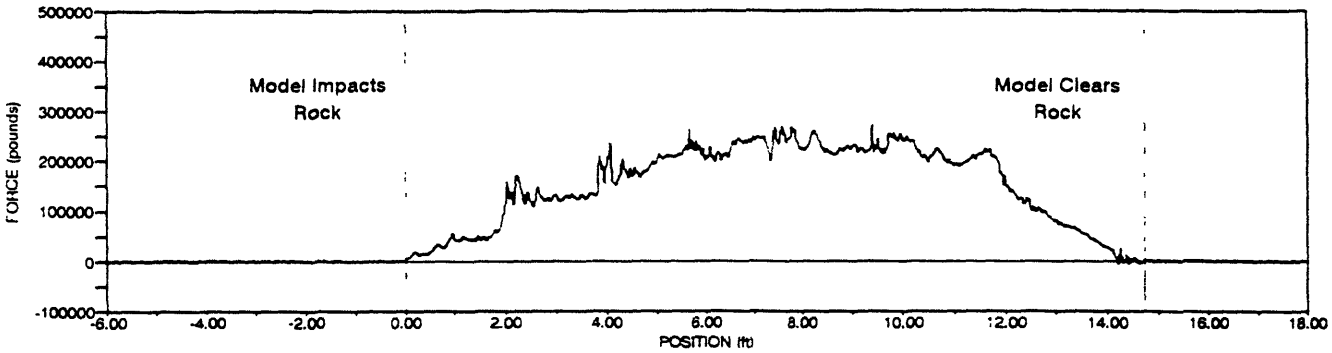

NSWC Experimental Horizontal Force vs. Distance along the Structure

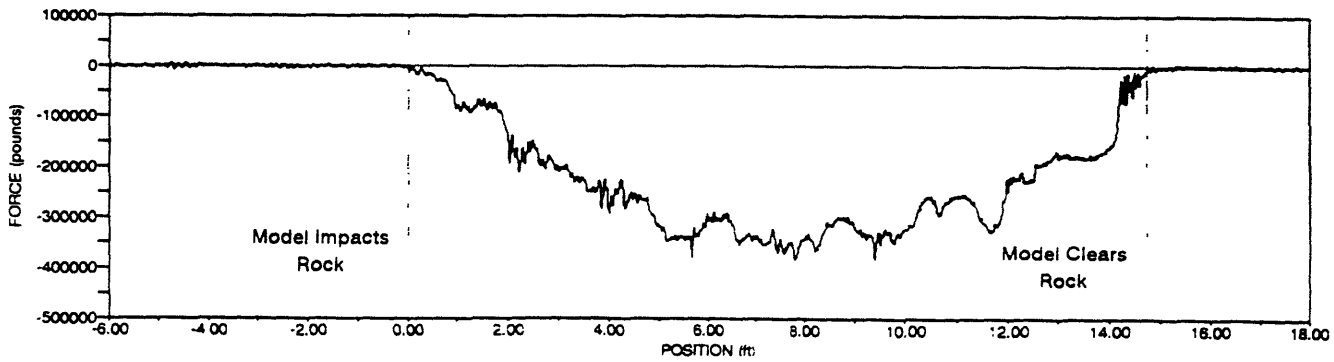

NSWC Experimental Vertical Force vs. Distance along the Structure

Figure 2.4. NSWC Grounding Test Rock Reaction Forces

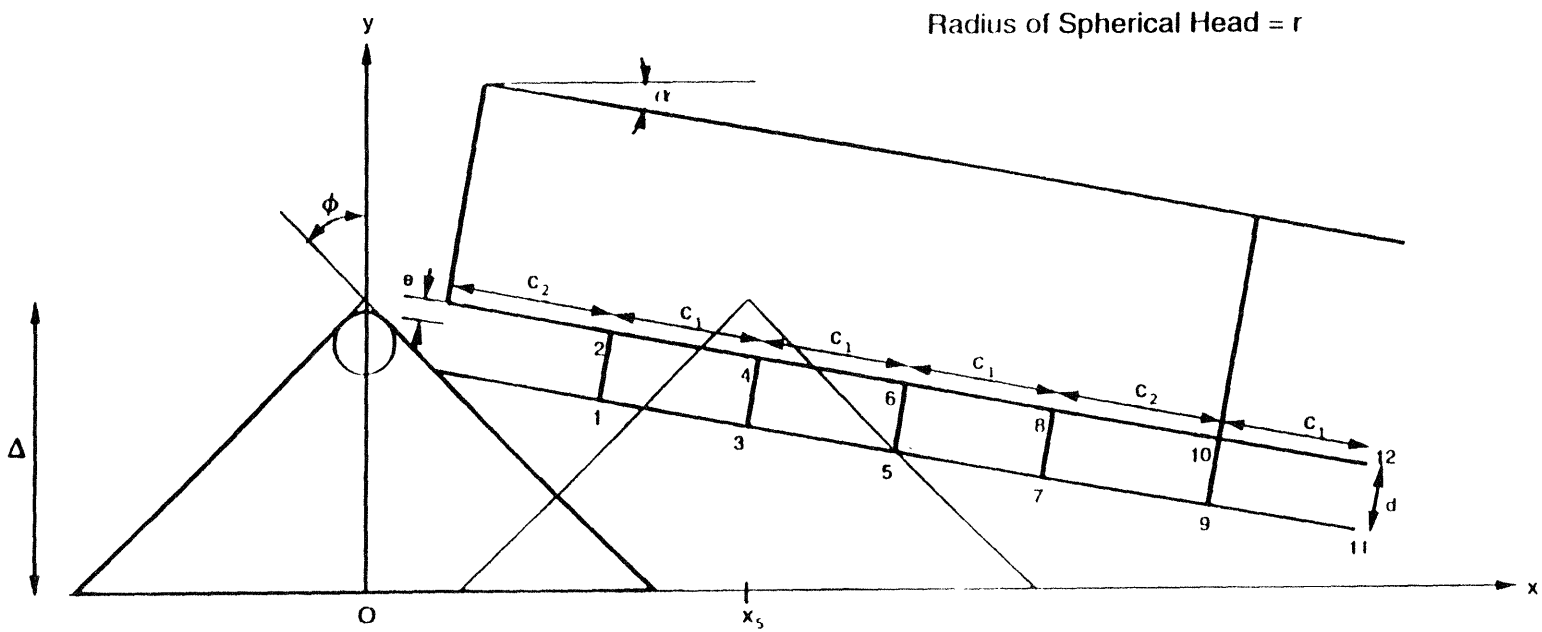

Figure 2.5. Global Coordinate System for Hull-Cone Interaction

Chapter 3

Contribution of Outer Plate to the Total Resisting Force

3.1 Introduction

In the NSWC grounding experiment, the outer plate is the first structural component that engages with the cone shaped rock. Because of the geometry of the arrangement, it is expected that the outer plate will be immediately ruptured after it first comes into contact with the cone. In the cutting process, we should expect two different phases to take place:

1. First, a cutting initiation phase, possibly including concertina tearing and other complicated failure modes
2. Finally, a steady state cutting phase, where the cone leaves a stable wake as it cuts through the plate.

In this chapter, we will develop theoretical models for both phases of the cutting process. The problem of cutting initiation through metal plates has been studied in the literature, e.g., Wierzbicki and Thomas [3] and Zheng [17]. Thus, the governing equation for the initiation phase shall be taken from Zheng [17] and modified to meet the geometric constraints of the problem. We will then proceed by deriving the governing equation for the steady state phase based on a curved flap model. The curved flap model will then be applied to the particular geometry of the NSWC grounding experiment. The boundaries of both initiation and steady state phases will be established based on geometrical assumptions supported by experimental observations. Finally, both initiation and steady state contributions will be added and the results summarized at the end of the chapter.

3.2 Outer Plate Cutting Initiation

3.2.1 Outer Plate Cutting Initiation Governing Equation

The problem of cutting initiation in metal plates has been studied by Wierzbicki and Thomas [3]. The governing equation for cutting initiation of a plate was derived by Zheng [17], as

$$F_{in}^{op} = \frac{4}{3}\sigma_0 t^{1.5} x^{0.5} \frac{(\sin\theta)^{0.5}}{\cos\theta} \cdot f_c \quad , \quad 0 \le x \le x_1 \tag{3.1}$$

where the variable x corresponds to the distance traveled by the conical wedge in the cutting process, t is the plate thickness, and σ_0 is the flow stress of the material, given as 46 ksi. The boundary x_1 is defined in figure 2.5 and shall be calculated in section 3.2.2. The friction correction factor f_c was calculated by Pippenger [5] as

$$f_c = \frac{1}{1 - \dfrac{\mu\cos\theta}{\cos\phi\sin\theta + \mu\cos\theta}} = 1 + \frac{\mu}{\cos\phi}\cot\theta \tag{3.2}$$

where ϕ is the cone apex angle measured from the vertical, and θ is the unknown split angle, as shown in figure 3.1. To obtain a closed form solution for the outer plate initiation force as a function of x we find the value of θ that minimizes the force in equation (3.1). Figure 3.2 shows a plot of the peak force with respect to θ, from which we infer that the optimum split angle is

$$\theta_{optimum}^{outer\ plate\ initiation} = 20 \quad \text{deg} \tag{3.3}$$

Substituting from equation (3.3) into (3.2), and then into (3.1), we eliminate the unknown θ and obtain the outer plate cutting initiation force as a function of x only, as desired. All numerical values of the various parameters of equation (3.1) are given in table A1.

3.2.2 Outer Plate Cutting Initiation Boundaries

The boundaries for the cutting initiation phase in the outer plate are determined from experimental experience in the following manner:

1. The initial value of the x-coordinate in equation (3.1) corresponds to the initial location of the cone axis, i.e. $x = 0$.
2. The final value of the x-coordinate in equation (3.1) corresponds to x_1, i.e. the location of the cone axis when the cone comes into contact with the first transverse frame, as shown in figure 2.5.

From the geometry in figure 2.5, we can express the boundary points as

$$\begin{aligned} x_i &= 0 \\ x_f &= c_2(\cos\alpha - \sin\alpha\tan\phi) = 24.16 \quad inches \end{aligned} \tag{3.4}$$

where all geometric constants are defined in figure 2.5 and given in table A1.

3.3 Outer Plate Steady State Cutting

3.3.1 Derivation of Outer Plate Steady State Cutting Force

3.3.1.1 Curved Flap Model Kinematics

Under steady state cutting, the outer plate is separated by the cone shaped wedge and bent up forming two curved flaps. The flaps bend along two inclined plastic hinges. The model is described in figure 3.3, where three distinct deformation zones are identified. First, the material undergoes membrane deformation in the vicinity of the tip zone. Second, the material undergoes bending deformation in the transient flaps. Then, the material is stretched when it enters the transition zones. Finally, upon leaving the transition zones, the material is compressed back and it may buckle near the stable flaps. No further material deformation occurs in the stable flaps.

3.3.1.2 Energy Dissipation

In the kinematically admissible deformation mechanism described above the material of the outer plate is first stretched, then cut, and finally removed by the cone shaped wedge in the out-of-plane direction. The velocity field depends on the parameters θ, B and R as defined in figure 3.4.

The steady state cutting force F_{ss}^{op} is determined from the upper bound theorem of plasticity

$$F_{ss}^{op} \cdot V = \int_S N_{\alpha\beta}\, \dot{\varepsilon}_{\alpha\beta}\, dS + \int_S M_{\alpha\beta}\, \dot{\kappa}_{\alpha\beta}\, dS \tag{3.5}$$

where V is the relative velocity of the plate relative to the cone, and $N_{\alpha\beta}$ and $M_{\alpha\beta}$ are the components of the membrane force and bending moment tensors. The strain and curvature rates $\dot{\varepsilon}_{\alpha\beta}$ and $\dot{\kappa}_{\alpha\beta}$ are calculated from the deformation modes described in

figure 3.3. The integration occurs over the whole deformed region. The material is characterized by the flow stress σ_0.

In the local curvilinear coordinate frame shown in figure 3.4 the condition of steady state is expressed mathematically as

$$V = \frac{d\xi}{dt} \tag{3.6}$$

Using the chain rule and equation (3.6) we obtain

$$\frac{d}{dt}(\quad) = \frac{\partial}{\partial \xi}(\quad) \cdot \frac{d\xi}{dt} = V \cdot \frac{\partial}{\partial \xi}(\quad) \tag{3.7}$$

And now we can eliminate differentiation with respect to time from the statement of the upper bound theorem of plasticity by substituting the result of equation (3.7) into equation (3.5). Hence

$$F_{ss}^{op} \cdot V = V \cdot \int_S N_{\xi\eta} \frac{\partial \varepsilon_{\xi\eta}}{\partial \xi} dS + V \cdot \int_S M_{\xi\eta} \frac{\partial \kappa_{\xi\eta}}{\partial \xi} dS \tag{3.8}$$

In equation (3.8), the first term of the right hand side corresponds to the membrane energy dissipation in the tip and transition zones, whereas the second term represents the energy dissipated via bending of the curved flaps.

Additionally, the following kinematic assumptions shall be made in order to simplify the problem:

1. Small bending effects in the near-tip zone are neglected
2. Plastic shear strain is ignored
3. Local necking in the near-tip zone is ignored, and the plate thickness is taken as constant.
4. The plate material obeys a plane stress von Mises yield condition

$$\sigma_{xx}^2 - \sigma_{xx}\sigma_{yy} + \sigma_{yy}^2 + 3\sigma_{xy}^2 = \sigma_0 \tag{3.9}$$

where σ_{xx}, σ_{yy} and σ_{xy} are the in-plane components of the stress tensor. The corresponding flow rule is

$$\left\{\begin{aligned} \dot{\varepsilon}_{xx} &= \dot{\lambda}\,(2\sigma_{xx} - \sigma_{yy}), \\ \dot{\varepsilon}_{yy} &= \dot{\lambda}\,(2\sigma_{yy} - \sigma_{xx}), \\ \dot{\varepsilon}_{xy} &= 3\dot{\lambda}\sigma_{xy} \end{aligned}\right\} \tag{3.10}$$

where $\dot{\lambda}$ is a scalar multiplier.

5. The plastic coupling between the bending moment $M_{\alpha\beta}$ and the membrane force $N_{\alpha\beta}$ is neglected in the near-tip zone and the transition zones. This assumption will overestimate the actual energy dissipated.

Making use of the above assumptions, let us now investigate the contributions of the different energy dissipation mechanisms in the curved flap model.

3.3.1.3 Bending Energy Rate

In the steady state cutting of the outer plate, bending is confined to the two inclined plastic moving hinges located in the transient flaps. The integration is performed over the area $l_\xi \times l_\eta$ containing the diagonal line OP as shown in figure 3.4, where l_ξ and l_η are the projections of the hinge length l into the ξ and η directions, respectively. In the local coordinate system $dS = d\xi \times d\eta$, and the limits of integration become $0 < \xi < l_\xi$ and $0 < \eta < l_\eta$. Also, from the geometry of the problem in figure 3.5

$$l_\eta = B + R\cos\phi \tag{3.11}$$

Let us consider one of the transient flaps in figure 3.4 and integrate first in the streamline direction ξ the second term of the right hand side of equation (3.8). Thus

$$\dot{E}_b = V\int_0^{l_\eta}\int_0^{l_\xi} M_{\xi\eta}\frac{d\kappa_{\xi\eta}}{d\xi}\,d\xi\,d\eta = V\int_0^{l_\eta} M_{\xi\eta}[\kappa_{\xi\eta}]\,d\eta \tag{3.12}$$

where $[\kappa_{\xi\eta}]$ is the curvature tensor jump across the hinge line. Due to the fact that the transient flaps form a cylindrical surface, there are no variations of the curvature jump in the circumferential direction η. Hence

$$\dot{E}_b = V\, l_\eta\, M_{\xi\eta}[\kappa_{\xi\eta}] \tag{3.13}$$

In the local coordinate system of the cylindrical transient flaps the curvature tensor is

$$\kappa_{\xi\eta} = \begin{bmatrix} \dfrac{1}{R\cos\theta} & 0 \\ 0 & 0 \end{bmatrix} \tag{3.14}$$

where R is the unknown radius of the stable flaps. It follows from the geometry of figure 3.4 that the radius of the transient flaps is obtained by dividing R by the cosine of the split angle θ, as is done in equation (3.14). Finally, substituting the results of equations (3.11) and (3.14) into equation (3.13), and taking into account that there are two transient flap zones in the model we obtain

$$\dot{E}_b = 2\, V\, M_0 \left(\frac{B + R\cos\phi}{R\cos\theta} \right) \tag{3.15}$$

where M_0 is the only non-zero component of the fully plastic bending moment tensor, in the circumferential direction; θ is the split angle and ϕ the cone angle. Using the yield condition described in equation (3.9) on the one-dimensional strain rate field we can express the yield moment M_0 in terms of the average flow stress σ_0, which is a well documented material property. Thus,

$$M_0 = \frac{2}{\sqrt{3}} \sigma_0 \frac{t^2}{4} \tag{3.16}$$

3.3.1.4 Near Tip Zone Membrane Energy Rate

In the curved flap model, membrane energy dissipation occurs both in the near-tip zone and also at the transition zones. In the near-tip plastic zone the following assumptions can be made, as suggested by Zheng [4]:

1. The strain rate component in the direction of the cone shaped wedge $\dot{\varepsilon}_{\xi\xi}$ should be zero. Otherwise, material would accumulate on the wedge tip, a hypothesis which contradicts experimental observations.
2. As a consequence of kinematic assumption (2) in section 3.3.1.3, the shear component $\dot{\varepsilon}_{\xi\eta}$ is also zero.

If we now apply the above kinematic restrictions to the yield condition in equation (3.9), and its corresponding flow rule relations in equation (3.10), we obtain

$$\sigma_{\xi\eta} = \frac{1}{\sqrt{3}}\sigma_0 \begin{bmatrix} 1 & 0 \\ 0 & 2 \end{bmatrix} \tag{3.17}$$

And by virtue of the chain rule and steady state conditions in equation (3.7), the strain rate tensor is

$$\dot{\varepsilon}_{\xi\eta} = \begin{bmatrix} 0 & 0 \\ 0 & V\dfrac{\partial \varepsilon_{\eta\eta}}{\partial \xi} \end{bmatrix} \tag{3.18}$$

Next, we consider the contribution of the near-tip zone membrane energy dissipation $\dot{E}_{m_1}$ to the first term of the right hand side of equation (3.8). Hence

$$\dot{E}_{m_1} = \int_S N_{\xi\eta}\,\dot{\varepsilon}_{\xi\eta}\,dS = t\int_S \sigma_{\xi\eta}\,\dot{\varepsilon}_{\xi\eta}\,dS \tag{3.19}$$

where $N_{\xi\eta} = t\,\sigma_{\xi\eta}$ and t is the plate thickness. The area of integration S is defined by the length of the near-tip plastic zone l_p in the streamline ξ-direction, and by the

boundary $\psi(\xi)$ in the η-direction. Then, substituting equations (3.17) and (3.18) into (3.19)

$$\begin{aligned}\dot{E}_{m_1} &= t\int_0^{l_p}\int_{-\psi}^{+\varphi}\left(\frac{1}{\sqrt{3}}\right)\sigma_0\begin{bmatrix}1 & 0\\ 0 & 2\end{bmatrix}\begin{bmatrix}0 & 0\\ 0 & V\dfrac{\partial\varepsilon_{\eta\eta}}{\partial\xi}\end{bmatrix}dS \\ &= \left(\frac{2}{\sqrt{3}}\right)t\,\sigma_0\,V\int_0^{l_p}\int_{-\psi}^{+\varphi}\frac{\partial\varepsilon_{\eta\eta}}{\partial\xi}\,dS\end{aligned} \tag{3.20}$$

Recall the definition of the strain rate tensor $\dot{\varepsilon}_{\xi\eta}$

$$\dot{\varepsilon}_{\xi\eta} = \frac{1}{2}\left(\dot{u}_{\xi,\eta}+\dot{u}_{\eta,\xi}\right) = V\cdot\frac{1}{2}\left(u_{\xi,\eta}+u_{\eta,\xi}\right) \tag{3.21}$$

Substituting equation (3.21) into equation (3.20) we obtain

$$\dot{E}_{m_1} = \left(\frac{2}{\sqrt{3}}\right)\sigma_0\,t\,V\int_0^{l_p}\frac{\partial}{\partial\xi}(u_\eta)\,d\xi \tag{3.22}$$

where u_η denotes the relative displacement in the near tip plastic zone. The maximum and minimum displacements are given by Zheng [4] and corrected by Simonsen [6] as

$$\begin{aligned}&u_\eta(\xi = l_p) = u_0 = 0.317\,R\cos\theta\left(1+0.55\,\theta^2\right)\\ &u_\eta(\xi = 0) = 0\end{aligned} \tag{3.23}$$

We can now substitute equation (3.23) into equation (3.22). Therefore,

$$\dot{E}_{m_1} = \frac{2}{\sqrt{3}}\,\sigma_0\,t\,V\,u_0 = 0.366\,V\,t\,\sigma_0\,R\cos\theta\left(1+0.55\,\theta^2\right) \tag{3.24}$$

And recalling the relationship between the fully plastic bending moment and the average flow stress expressed in equation (3.16), we arrive at the following expression for the contribution of the near tip plastic zone to the membrane energy dissipation:

$$\dot{E}_{m_1} = 1.27\, M_0\, V \frac{R}{t} \cos\theta \left(1 + 0.55\, \theta^2\right) \tag{3.25}$$

3.3.1.5 Membrane Energy Rate in the Transition Zones

The transition zones between the transient and the stable flaps are in effect toroidal surfaces where the material is first stretched and finally compressed upon entering the stable flaps. In such transition zones, the following kinematic assumptions are suggested by Zheng [4]:

1. Due to rotational symmetry of the shell, the shear strain $\varepsilon_{\xi\eta}$ vanishes.
2. The arc length of the transient flaps is equal to the arc length of the stable flaps.
3. The material is inextensible in the circumferential direction, i.e. $\varepsilon_{\eta\eta} = 0$.

After applying the above kinematic restrictions to the yield condition in equation (3.9) and the corresponding flow rule of equation (3.10), the stress and strain rate tensors become

$$\sigma_{\xi\eta} = \frac{1}{\sqrt{3}} \sigma_0 \begin{bmatrix} 2 & 0 \\ 0 & 1 \end{bmatrix} \tag{3.26}$$

and

$$\dot{\varepsilon}_{\xi\eta} = \begin{bmatrix} V \dfrac{\partial \varepsilon_{\xi\xi}}{\partial \xi} & 0 \\ 0 & 0 \end{bmatrix} \tag{3.27}$$

Next, we let us consider the contributions of the two transition zones to the membrane energy dissipation term in the right hand side of equation (3.8). Hence

$$\dot{E}_{m_2} = 2 \int_S N_{\xi\eta}\, \dot{\varepsilon}_{\xi\eta}\, dS = 2\, t \int_S \sigma_{\xi\eta}\, \dot{\varepsilon}_{\xi\eta}\, dS \tag{3.28}$$

where $N_{\xi\eta} = t\, \sigma_{\xi\eta}$ and t is the plate thickness. The area of integration S is defined in the local coordinate system by the streamline coordinate boundary C and $0 < \eta < l_\eta$ in the

circumferential direction, where l_η is defined in equation (3.11). Then, substituting equations (3.26) and (3.27) into (3.28)

$$\dot{E}_{m_2} = 2\,t \cdot V \frac{2}{\sqrt{3}}\,\sigma_0 \int_0^{l\eta} \int_{-c}^{c} \frac{\partial \varepsilon_{\xi\xi}}{\partial \xi}\, d\xi\, d\eta = 2\,t \cdot V \frac{2}{\sqrt{3}}\,\sigma_0 \int_0^{l\eta} \varepsilon_{\xi\xi}\, d\eta \qquad (3.29)$$

The strain in the transition zones was calculated by Zheng [4] and corrected by Simonsen [6] for a similar geometry as

$$\varepsilon_0(\eta) = 0.29\,\theta \sin\theta \frac{\cos\,\theta/2}{\cos\,\theta} \cdot \frac{\eta}{R} \qquad (3.30)$$

After substituting for the strain into equation (3.29) and integrating we obtain

$$\dot{E}_{m_2} = 1.16\,V\,M_0\,\theta \sin\theta\,\frac{\cos\,\theta/2}{\cos\theta} \cdot \frac{(R\cos\phi + B)^2}{R\,t} \qquad (3.31)$$

where M_0 is defined in equation (3.17).

3.3.1.6 Theoretical Outer Plate Steady State Cutting Force without Friction

Having so far calculated the contributions of the different energy dissipation modes, we can now substitute from equations (3.15), (3.25) and (3.31) into the expression for the steady state upper bound theorem of plasticity in equation (3.8). Hence

$$\frac{F_{ss}^{op}}{M_0} = 2 \cdot \frac{B + R\cos\phi}{R\cos\theta} + 1.27\,\frac{R}{t}\cos\theta\left(1 + 0.55\,\theta^2\right) + 1.16\,\theta\sin\theta\,\frac{\cos\theta/2}{\cos\theta} \cdot \frac{(R\cos\phi + B)^2}{R\,t} \qquad (3.32)$$

where we have eliminated V and have non-dimensionalized by the fully plastic bending moment M_0. In equation (3.32) the unknowns are the outer plate cutting force F_{ss}^{op}, and the stable flap rolling radius R and the wedge shoulder B, both of which are defined in

figure 3.5. Additionally, the split angle θ is also a free parameter which we need to determine. Therefore, at this point we have one equation for four unknowns. The immediate task is to identify another three equations relating the four unknowns.

3.3.1.7 Geometric Relation between *R* and *B* for a Conical Wedge

Figure 3.5 shows the geometry of the side view interaction between the outer plate and the cone in the curved flap model. From simple geometric arguments we can establish the following relation between *R* and *B*

$$B = \frac{h - R\,(1 - \sin\phi)}{\cot\phi} \tag{3.33}$$

where *h* is the vertical distance between the vertex of the cone and the undeformed outer plate, as shown in figure 3.5. In the next section, we shall express *h* as a function of x. At any rate, it is sufficient to say now that *h* is a known quantity that can be derived from the geometry of the problem.

3.3.1.8 Closed Form Solution for the Outer Plate Steady State Cutting Force

In order to establish a third relation between the four unknowns of the problem, it is necessary to postulate that the rolling radius *R* adjusts itself so as to minimize the cutting force. That is, first we substitute for *B* from equation (3.33) into equation (3.32), and then we calculate the analytical minimum of equation (3.32), imposing the condition $\frac{dF_{ss}^{op}}{dR} = 0$. Then

$$\frac{R}{h} = \sqrt{\frac{\dfrac{2}{\cot\phi\,\cos\theta}\cdot\dfrac{t}{h} + 1.16\,\theta\sin\theta\,\dfrac{\cos\theta/2}{\cos\theta\;\cot^2\phi}}{1.27\,\cos\theta\left(1 + 0.55\,\theta^2\right) + 1.16\,\theta\sin\theta\,\dfrac{\cos\theta/2}{\cos\theta}\cdot\left[\cos\phi - \tan\phi\,(1 - \sin\phi)\right]^2}} \tag{3.34}$$

In equation (3.34), R is expressed as a function of h, which is a known geometric quantity. Therefore, we can now substitute from equations (3.33) and (3.34) into equation (3.32) and eliminate B and R as unknowns variables, leaving the plastic force F_{ss}^{op} as a function of the split angle θ only.

3.3.1.9 Friction Contribution to the Outer Plate Steady State Cutting Force

The next step in our derivation is to include the effect of friction on the plastic cutting force. Such an effect was investigated by Zheng [17] and perfected by Pippenger [5], who found a friction correction factor for a problem of similar geometry of the form

$$f_c = \frac{1}{1 - \dfrac{\mu \cos\theta}{\cos\phi \sin\theta + \mu \cos\theta}} = 1 + \frac{\mu}{\cos\phi} \cot\theta \qquad (3.35).$$

The total plastic force is then found by multiplying equation (3.32) by equation (3.35) such that

$$Tot\ F_{ss}^{op} = F_{ss}^{op} \cdot f_c \qquad (3.36)$$

Let us recall that after the last few substitutions performed into equation (3.32), we have reduced the number of variables, so that $F_{ss}^{op} = f(\theta, h(x))$ only. Hence, the final step consists of determining a relation between the total force in equation (3.36) and the plate split angle θ. In figure 3.6, the total plastic force including the friction effect is plotted against the split angle θ. It is postulated that the split angle is such that it minimizes the total force. From the graph in figure 3.6, it can be inferred that the optimum split angle is 10 degrees. However, because of the transverse framing, it is impossible to conceive geometrically a crack tip far enough ahead of the cone to possibilitate such a small split angle. Hence, based on geometric constraints, a minimum split angle of 20 degrees is postulated. In figure 3.6, we observe that at 20 degrees the force level is a quasi-minimum, and therefore the violation of the criterion of minimum force for the selection of the split angle is of small order. Consequently,

$$\theta_{optimum}^{outer\ plate\ steady-state} = 20 \text{ deg} \tag{3.37}$$

Finally, we have eliminated the unknown parameters B, R, and θ , such that now F_{ss}^{op} is a function of known geometric parameters, e.g. h, only. The geometric characteristics of F_{ss}^{op} are explored in the next section.

3.2.2 Geometry of Outer Plate Steady State Cutting

In section 3.2.1, the governing equation for the contribution of the steady state cutting of the outer plate to the total resisting force was derived as equation (3.36). The task now is to find the dependency of this theoretical force with respect to the distance traveled by the structure relative to the cone. In other words, the task is to establish the history of the force in order to compare it to the experimental results of the NSWC grounding experiment shown in figure 2.4.

First, let us define a coordinate system for the problem. Such coordinate system is shown in figure 2.5, where the origin O corresponds to the location of the axis of the cone at the time of the first contact with the leading edge of the structure. The y-axis runs parallel to the cone axis, and the x-axis is parallel to the ground. By symmetry, we will consider that the cone advances with respect to an stationary structure, whereas in reality the process occurs viceversa.

Having defined the coordinate system, let us now be concerned with establishing the x-coordinate dependency of the parameters that determine the resisting force in equation (3.36), namely the flap rolling radius R and the wedge shoulder B. In equation (3.33), it was shown that B and R are related via the quantity h, the vertical distance from the vertex of the cone to the undeformed outer plate. Because of the tilt angle α, h becomes a function of x. Then, by virtue of equation (3.33), both B and R also become functions of x. Hence, the outer plate steady state cutting force in equation (3.36) is a function of x.

Consider figure 2.5. In the x-y plane, the outer plate is described by the line

$$y_{op} = m_1 - x \tan\alpha \qquad , \qquad x_{t0} \le x \le x_{t11} \tag{3.38}$$

where α is the tilt angle of the plate relative to the ground, x_{t0} is the location of the leading edge of the outer plate, and x_{t11} is the location of the trailing edge of the outer plate, as shown in figure 2.5. From geometrical considerations, the y-intercept m_1 can be expanded as

$$m_1 = \Delta_1 + (d-e)(\sin\alpha \tan\phi - \cos\alpha) + r\left(\frac{1}{\cos\phi} - \tan\phi\right)\tan\alpha \tag{3.39}$$

where all the geometric parameters are given in table A1. Substituting from the values in table A1 into equation (3.39), we obtain

$$m_1 = 25.375 \quad inches. \tag{3.40}$$

From the geometry of the problem h can be defined as

$$h = \Delta - y_{op} = \Delta - m_1 + x \tan\alpha \tag{3.41}$$

after substituting for y_{op} from equation (3.38). Note that the height of the cone Δ and the height of the cone shaped rock Δ_1 are different because of the rounded tip of the rock. In fact, we can relate both quantities from simple geometry such that

$$\Delta_1 = \Delta + r\left(1 - \frac{1}{\sin\theta}\right) \tag{3.42}$$

where r is the rounded tip radius and θ the cone angle. The values for both Δ and Δ_1 are listed in table A1 as 38.9 inches and 36.0 inches, respectively.

Thus, we have determined h as $h(x)$, and having done so we can substitute into equation (3.33). Then, we have expressed the total force as a function of x only, which can easily be implemented in the computer.

3.2.3 Outer Plate Steady State Cutting Boundaries

Because of the geometry of the problem as shown in figure 2.5, rupture of the outer plate occurs immediately after contact is made between the cone and the outer plate leading edge. Thus, before the process reaches steady state, a certain degree of cutting initiation is to be expected, Zheng [17]. In the present analysis, the length of the initiation phase is assumed to be the distance from point O to station x_1 in figure 2.5. In other words, steady state cutting of the outer plate begins at the point of contact between the cone and the first transverse frame.

In addition, the final location after which the steady state force drops linearly to zero is assumed to be the location of the cone axis when the cone is tangent to the outer plate trailing edge, i.e. station x_{11} in figure 2.5.

By considering the geometry of figure 2.5, we can expand the boundary points x_i^{op} and x_f^{op} as

$$\begin{aligned} x_i^{op} &= x_1 = c_2(\cos\alpha - \sin\alpha \tan\phi) \\ x_f^{op} &= x_{11} = l\,(\cos\alpha - \sin\alpha \tan\theta) \end{aligned} \tag{3.43}$$

Substituting for the numerical values of the various parameters from table A1, we obtain $x_i^{op} = 24.16 \quad inches$ and $x_f^{op} = 134.6 \quad inches.$

3.4 Summary of Outer Plate Contribution to the Total Resisting Force

In this chapter we have investigated the contribution of the outer plate to the total resisting force in both initiation and steady state modes. This contribution is plotted along the length of the model structure in figure 3.7. Note that in figure 3.7 we can distinguish the following intervals:

$0 \leq x \leq 24.16 \quad inches$	Initiation Phase
$24.16 \leq x \leq 134.6 \quad inches$	Steady State Phase
$134.6 \leq x \leq 170 \quad inches$	Contribution drops linearly to zero

Table 3.1: Summary of Outer Plate Contribution to the Total Resisting Force

In table 3.1, the final value of *170 inches* corresponds to the overall length of the model structure. We observe that the initiation force is proportional to the square root of x, as we should expect from equation (3.1). However, the steady state component is linear with x. Such a linear dependence is also expected from the theory developed in the previous section. Recall from equation (3.41) that h is linear in x. Also, via the geometric relation in equation (3.33), B and R are linear in h, and hence linear in x. Finally, considering equation (3.32) we conclude that since the steady state force is linear in B and R, it should also be linear in x.

All calculations were performed using MATLAB software. A hard copy of the source code is included in the Appendix.

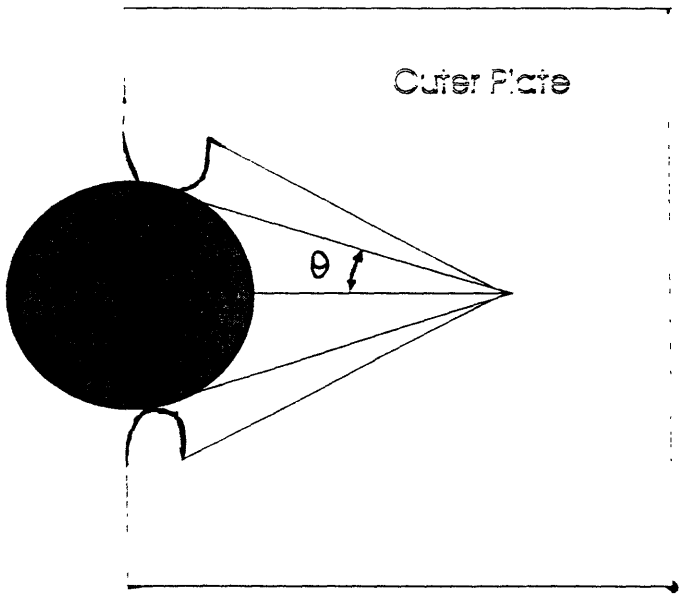

Figure 3.1. Aerial View of Cone Cutting through Outer Plate

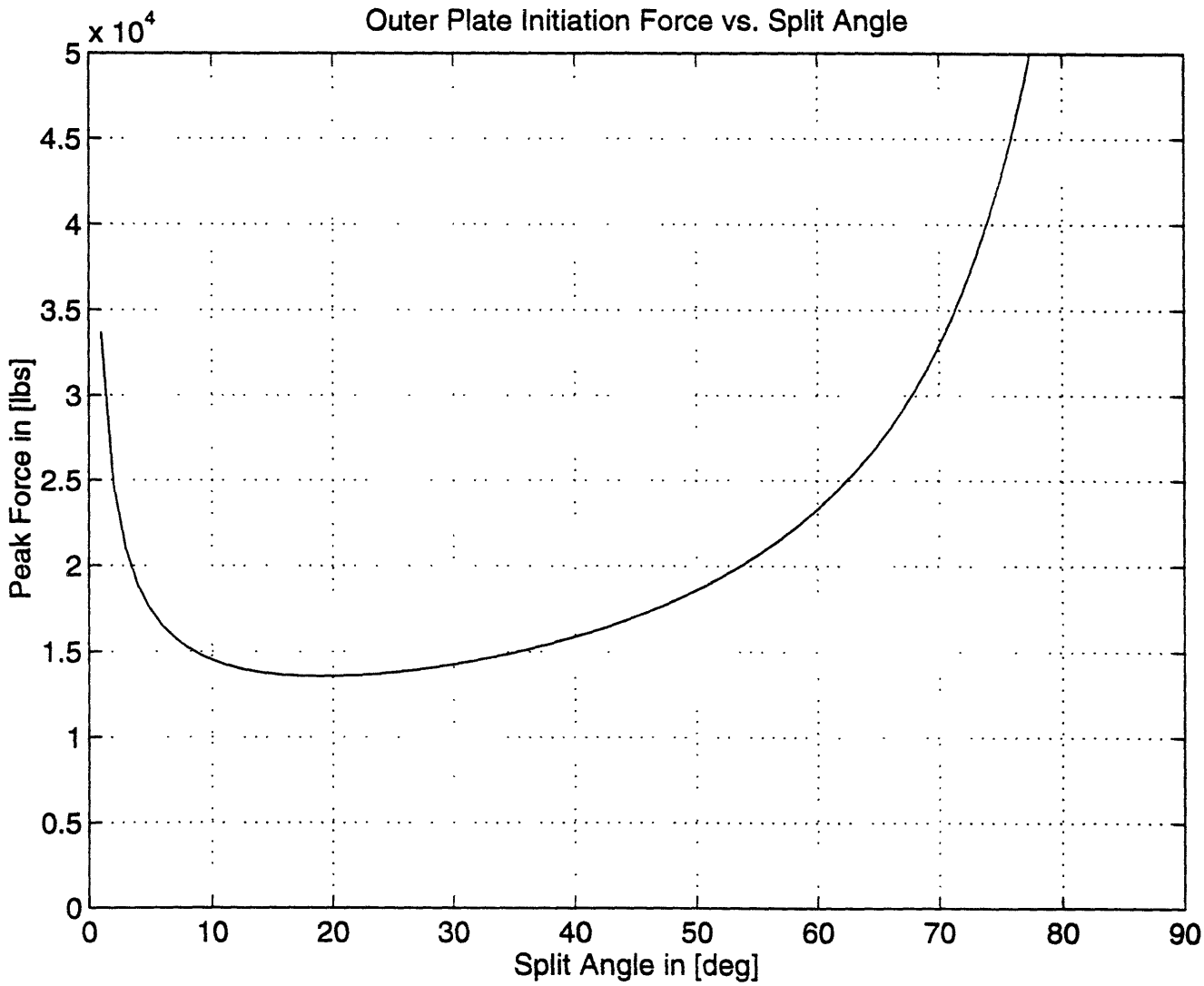

3.2. Outer Plate Initiation Force vs. Split Angle

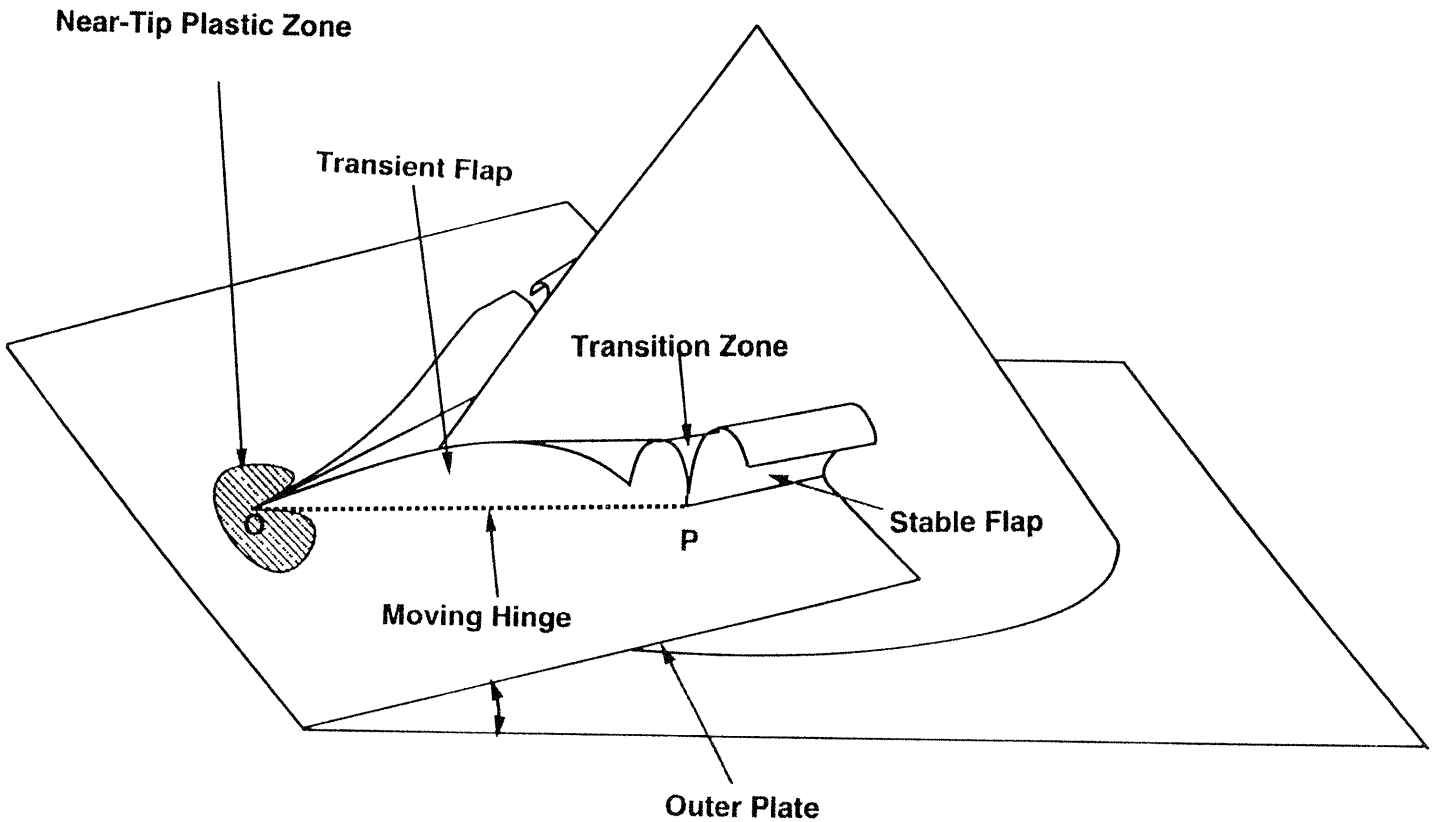

Figure 3.3. Curved Flaps Model Geometry

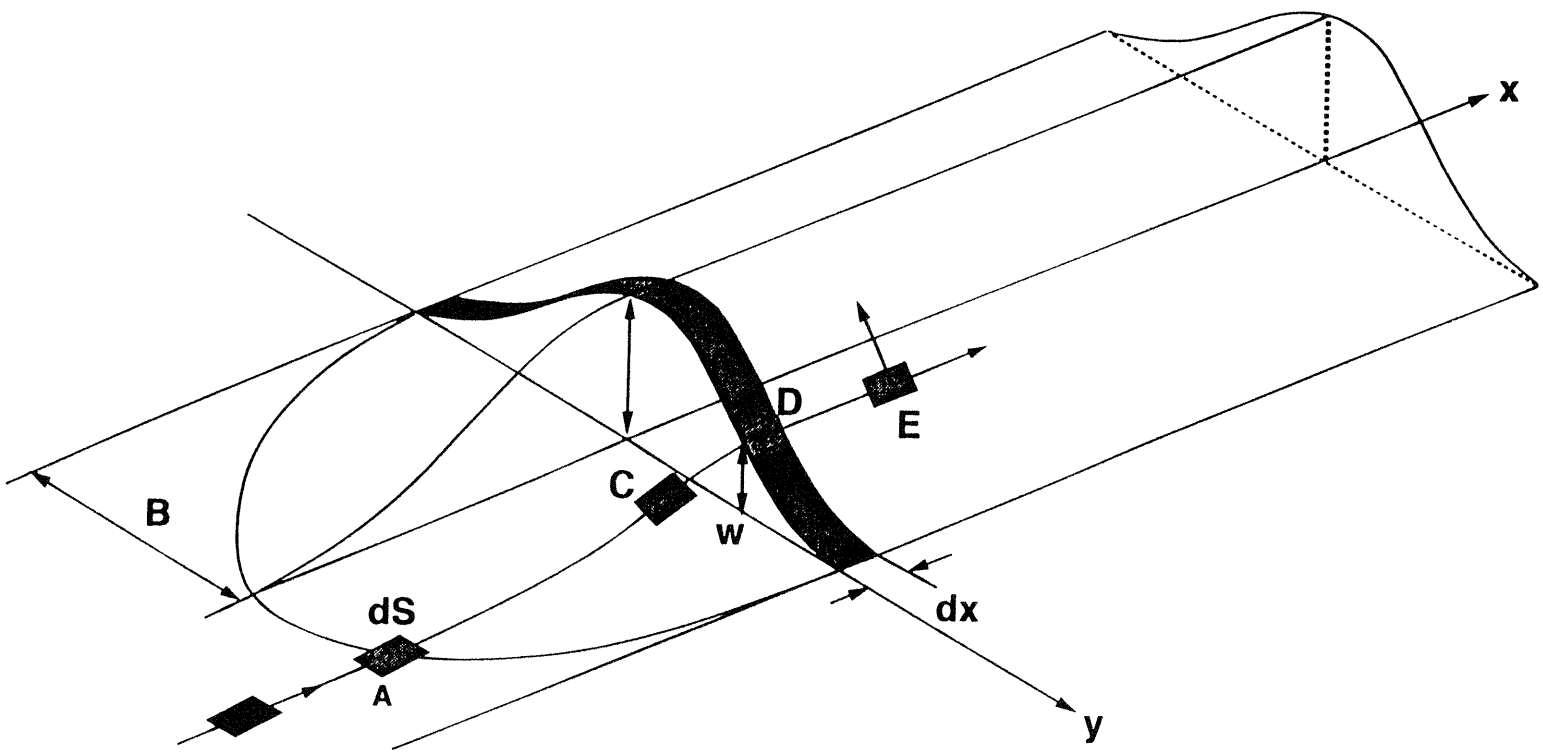

Figure 3.4. Local Coordinate System for Curved Flaps Model

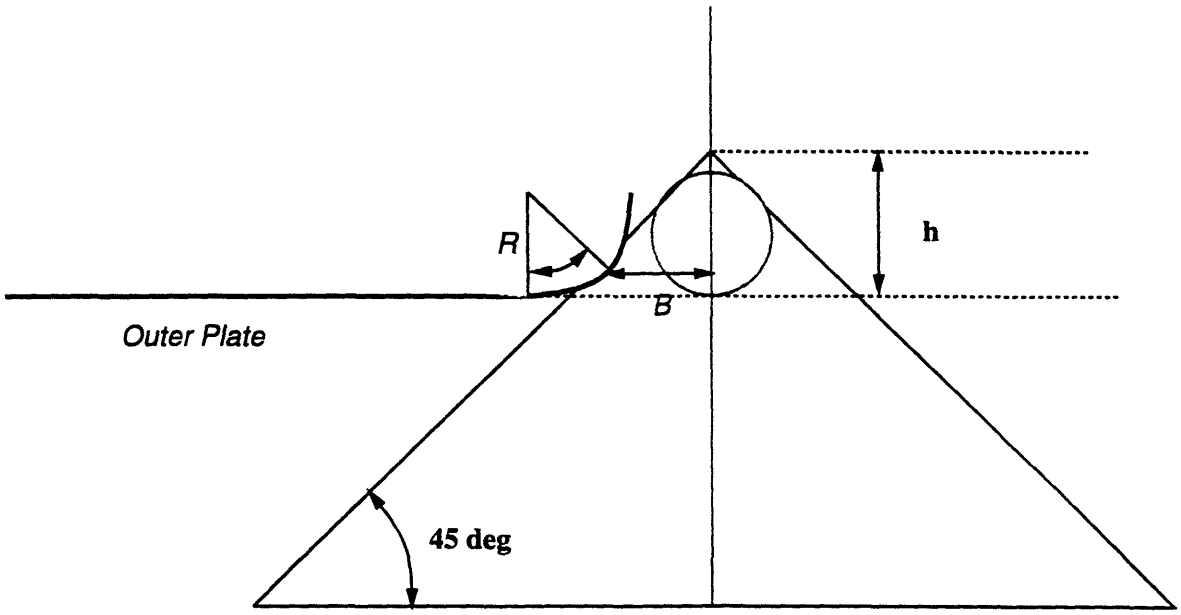

Figure 3.5. Side View of Cone-Outer Plate Interaction

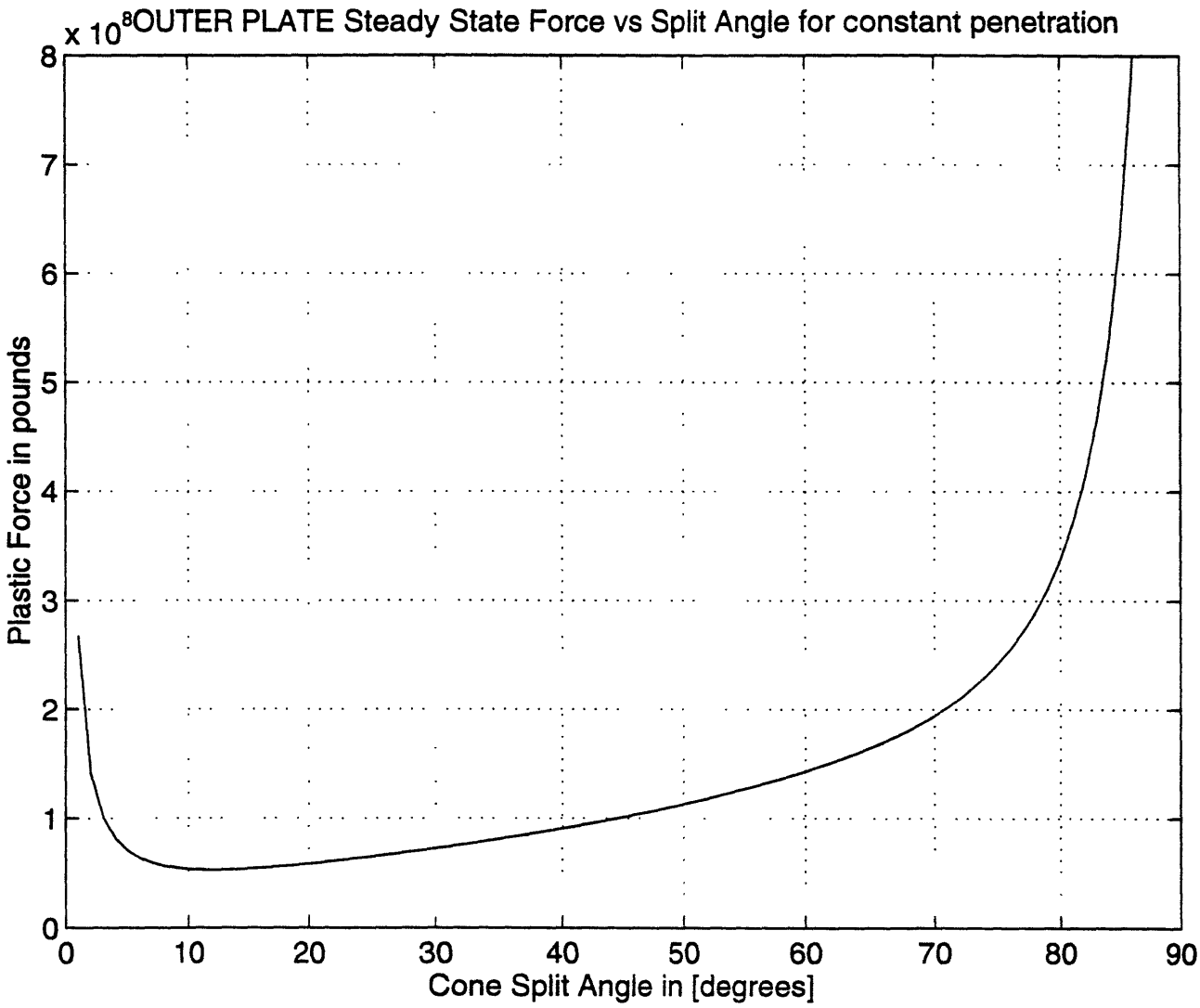

Figure 3.6. Outer Plate Steady State Force vs. Split Angle

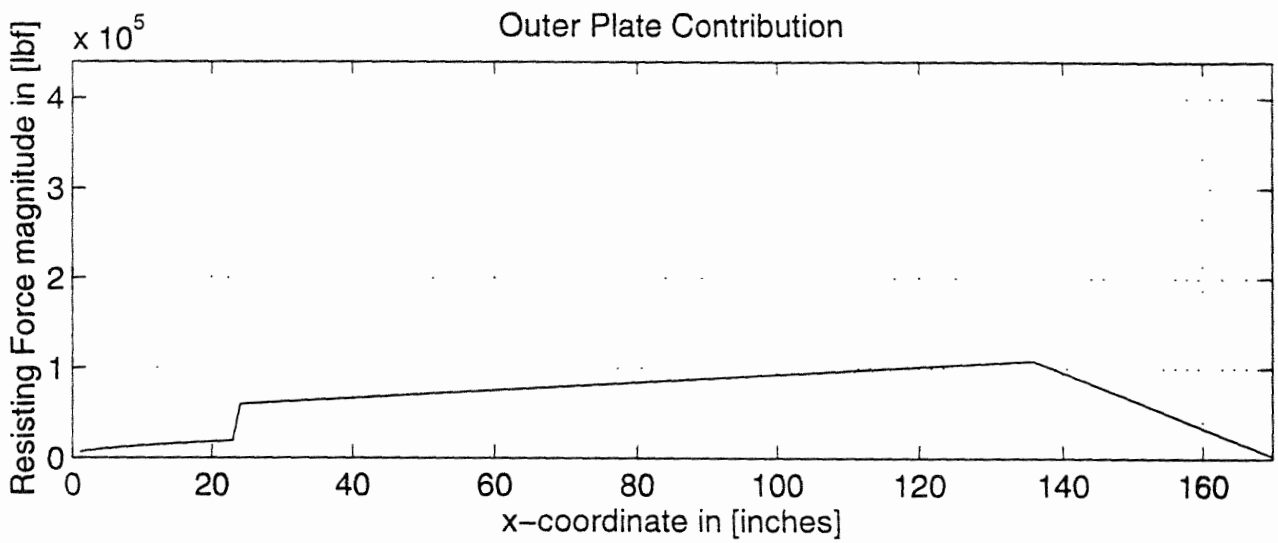

Figure 3.7. Theoretical Outer Plate Contribution to the Total Resisting Force

Chapter 4

Contribution of Inner Plate to the Total Resisting Force

4.1 Introduction

The mechanics of the cutting process of the inner plate are significantly different from the outer plate because of the geometric configuration of the structural model. In the case of the outer plate, the proposed theoretical model developed in chapter 3 was a curved flap model. The reasoning for such a choice of model was based on the fact that rupture of the outer plate is immediate upon contact, and hence the problem becomes analogous to that of a wedge indentation through a plate.

In the case of the inner plate, however, rupture is by no means immediate. As shown in figure 2.5, the leading edge of the inner plate is higher above the ground than the tip of the cone at the initial point of contact. As the cone penetrates the structure, it begins to approach the inner plate because of the tilt angle of the plate. Eventually contact is made at the location x_c. From this point on, the cone pushes up the inner plate until the upward penetration generated strain reaches critical value. At this point x_r, rupture occurs, relieving much of the inner plate resisting force.

In addition, experimental evidence gained from NSWC Grounding Tests corroborates that the initiation of rupture in the inner plate is generated through cracks propagating ahead of the cone in the outer plate, and running up through transverse frames to meet the inner plate. In fact, according to NSWC experimental observations [1], inner plate rupture

occurs when the vertical penetration of the cone into the inner plate exceeds 0.4 times the double hull height.

After the initial point of rupture x_r, the inner plate enters a steady state cutting phase, in a manner analogous to the outer plate. However, in order to capture the failure behavior described above, it is necessary to consider a different approach for the derivation of the governing equation of the steady state inner plate contribution to the total resisting force. This new approach is based on a straight flap model.

In this chapter, we shall develop theoretical models for both phases of the inner hull cutting process.

4.2 Inner Plate Cutting Initiation

4.2.1 Inner Plate Cutting Initiation Governing Equation

Consider the frontal view of the structure in figure 4.1. We observe that the vertical penetration into the inner plate is constrained by the presence of the longitudinal girders A and B. We can define the angle β as

$$\tan\beta = \frac{\delta}{d} \tag{4.1}$$

where δ is the penetration into the inner plate and d is the double hull height, which is approximately also half of the horizontal separation between the longitudinal girders. Under fully plastic conditions, the resisting force can be expressed, as derived by Simonsen [6], as

$$F^{ip} = \frac{\sigma_0\, t\, \delta}{\cos\alpha} \tag{4.2}$$

where t is the plate thickness, and the fully plastic load is projected onto the horizontal by dividing by the cosine of the tilt angle α. Finally, by including the appropriate friction correction factor into equation (4.2) we obtain

$$F^{ip} = \frac{\sigma_0 \, t \, \delta}{\cos\alpha} \left(\frac{1}{1 - \left(\frac{\mu}{\cos\alpha \left(\sin(\alpha+\beta) + \mu \cos(\alpha+\beta) \right)} \right)} \right) \quad , \quad x_c \le x \le x_r \qquad (4.3)$$

where the friction coefficient μ=0.3, x_c is the initial contact point between the cone and he inner plate, and x_r is the point at which the inner plate ruptures.

4.2.2 Geometry of Inner Plate Cutting Initiation

In determining the geometry of the inner plate cutting process, the goal is once more to establish the variation of the force along the length of the structural model. As for the case of the outer plate, we will once more refer to the coordinate system in figure 2.5. Then, we can describe the inner plate in the x-y plane by the line

$$y_{ip} = m_2 - x \tan\alpha \quad , \quad x_{t0'} \le x \le x_{t12} \qquad (4.4)$$

where α is the tilt angle, and $x_{t0'}$ and x_{t12} are the leading and trailing edges of the inner plate. From the geometry of figure 2.5, the y-intercept m_2 can be expanded as

$$m_2 = \Delta_1 + (d-e)(\sin\alpha \tan\phi - \cos\alpha) + \frac{d}{\cos\alpha} + r\left(\frac{1}{\cos\phi} - \tan\phi\right)\tan\alpha \qquad (4.5)$$

where all relevant geometric parameters are defined in figure 2.5 and their values given in table A1. Substituting from table A1 into equation (4.5) we obtain

$$m_2 = 40.25 \quad inches \qquad (4.6)$$

Now, we can express the penetration into the inner plate δ as a function of x, since

$$\delta = \Delta_1 - y_{ip} = \Delta_1 - m_2 + x \tan\alpha \qquad (4.7)$$

where Δ_1 is the height of the cone (not the height of the rock).

If we now substitute for δ from equation (4.7) into equation (4.3), we will have expressed the force as a function of x.

4.2.3 Inner Plate Cutting Initiation Boundaries

The contribution of the inner plate cutting initiation to the total resisting force starts at the point where the cone first makes contact with the inner plate. This location can be derived geometrically from figure 2.5 as

$$x_c = r\left(\frac{1}{\cos\phi} - \tan\phi - \frac{\cos\alpha - 1}{\tan\alpha}\right) + \frac{d}{\sin\alpha} + (d-e)\cos\alpha\left(\tan\phi - \frac{1}{\tan\alpha}\right) \quad (4.8)$$

Substituting from table A1 we calculate

$$x_c = 33.16 \quad inches \quad (4.9)$$

Empirical observations on NSWC tests revealed that rupture occurred when the penetration exceeded 0.4 times the double hull height. This condition is expressed mathematically as

$$\delta = (0.4)\, d \quad (4.10)$$

Substituting for δ into equation (4.7) and solving for x we obtain

$$x_r = \frac{(0.4)\, d - \Delta_1 + m_2}{\tan\alpha} \quad (4.11)$$

and substituting from table A1 we calculate

$$x_r = 78.15 \quad inches \quad (4.12)$$

4.3 Inner Plate Steady State Cutting

4.3.1 Derivation of Inner Plate Steady State Cutting Force

4.3.1.1 Straight Flaps Model Kinematics

The deformation pattern of the inner plate observed in the NSWC Grounding Experiment cannot be accurately described by the curved flaps model used for the outer plate (see section 3.3.1.1). In the case of the inner plate, experimental evidence corroborates that the generated flaps do not roll away from the cone. Based on this fact, a new approach in the form of a straight flaps model was implemented.

The characteristic geometry of the straight flaps model is depicted in figure 4.2. The deformation of the inner plate is symmetric on both sides of the cone, hence only one side needs to be considered for analysis. As the plate moves past the cone with a certain velocity V, it eventually ruptures at the center, so that the line OQRS defines a free edge. The area enclosed by OPRQO is assumed to undergo plastic membrane strains with rupture.

A material streamline is shown in figure 4.2. At any given point along the trajectory, a local coordinate system is defined, where the coordinate ξ is directed in the streamline direction and the coordinate η is perpendicular to the streamline direction. The material element is undeformed until it reaches the line OP. The, as the material element passes through the triangular region OPR, it is stretched. As discussed by Zheng [4], it is unlikely that the plate recompress to a straight flap, but rather it will tend to buckle as shown in figure 4.2.

4.3.1.2 Energy Dissipation

Because of the large membrane strains present in the triangular region OPR in figure 4., the bending energy dissipated by the hinge line OP becomes a second order effect, and hence it shall be ignored. Hence, the statement of the steady state upper bound theorem of plasticity in equation (3.6) becomes

$$F_{ss}^{ip} \cdot V = V \cdot \int_S N_{\xi\eta} \frac{\partial \varepsilon_{\xi\eta}}{\partial \xi} dS \tag{4.13}$$

Note that in equation (4.13) the bending energy dissipation term has been omitted in accordance to the assumption stated above.

Furthermore, let us assume that lengths of the lines PR and PQ are equal and that the transverse component of strain in the η direction vanishes. Shear strain is considered via an equivalent strain rate formulation. Therefore, the two dimensional strain rate tensor under the steady state condition in (3.5) becomes

$$\dot{\varepsilon}_{\alpha\beta} = \dot{\varepsilon}_{eq} = V \cdot \frac{\partial}{\partial \xi}\left[\varepsilon_{eq}\right] \tag{4.14}$$

Next, if we substitute for the strain tensor into the von Mises yield condition in equation (3.7) we obtain

$$N_{\xi\eta} = t\,\sigma_{\xi\eta} = t\,\frac{1}{\sqrt{3}}\sigma_0 \begin{bmatrix} 2 & 0 \\ 0 & 0 \end{bmatrix} \tag{4.15}$$

Now we can substitute from equations (4.14) and (4.15) into (4.13). Thus

$$F_{ss}^{ip} = 2 \cdot \frac{2}{\sqrt{3}}\sigma_0\, t \int_0^{\eta_{max}} \int_{-c}^{+c} \frac{\partial \varepsilon_{eq}}{\partial \xi}\, d\xi\, d\eta = \frac{4}{\sqrt{3}}\sigma_0\, t \int_0^{\eta_{max}} \varepsilon_{eq}(\eta)\, d\eta \tag{4.16}$$

where the factor of 2 comes from considering the 2 flaps on both sides of the cone. If we assume a buckled flap wake and therefore neglect strain reversal, we can express the strain as

$$\varepsilon_{eq}(\eta) = \frac{u(\eta)}{l(\eta)} \tag{4.17}$$

where $u(\eta)$ is the stretching given by the gap between PR and PQ in figure 4.2, and $l(\eta)$ is the original length of the fiber being stretched. From the geometry of figure 4.2, we can expand the gap opening and the fiber length as

$$\begin{aligned} l(\eta) &= \eta \cot\theta \\ u(\eta) &= \eta \sqrt{(1-\cos\beta)^2 \sin^2\theta + (1-\cos\theta)^2 \sin^2\beta} \end{aligned} \tag{4.18}$$

where β is defined in equation (4.1), and $\eta_{\max} = \dfrac{\delta}{\tan\phi}$ is the length of the straight flap attached to the cone. Substituting from equations (4.18) into (4.17) and (4.16), and integrating we obtain the expression for the steady state inner plate cutting force as

$$F_{ss}^{ip} = \frac{4}{\sqrt{3}}\sigma_0 t \frac{\delta}{\tan\phi}\sqrt{(\tan^2\theta + 1/4)\left[(1-\cos\beta)^2 \sin^2\theta + (1-\cos\theta)^2 \sin^2\beta\right]} \tag{4.19}$$

where we have applied the relevant functional relation for the equivalent strain in equation (4.17), as suggested by Simonsen [6]. Also, in this case, the angle β, i.e. the rotation of the flaps with respect to the horizontal, is constrained by the cone angle ϕ, such that since the flaps are attached to the cone β=ϕ, as shown in figure 4.3.

4.3.1.3 Friction Contribution to the Steady State Cutting Force

The friction correction factor used for the steady state cutting of the inner plate is the same as the one used for the outer plate in equation (3.35). Therefore, the total inner plate resisting force becomes

$$Tot\ F_{ss}^{ip} = F_{ss}^{ip} \frac{1}{1 - \dfrac{\mu\cos\theta}{\cos\phi\sin\theta + \mu\cos\theta}} \tag{4.20}$$

4.3.1.4 Closed Form Solution for the Inner Plate Steady State Cutting Force

In equation (4.20) the inner plate cone splitting angle θ is an unknown parameter. In order to eliminate θ as an unknown, we plot the total inner plate force in equation (4.20)

with respect to θ . This plot is shown in figure 4.4, from which we can observe that there is no value of θ that minimizes the total inner plate force, other than zero, the trivial solution. Thus, we are forced to estimate the splitting angle from the geometry of the steady state cutting of the inner plate. In reality, the splitting angle is constrained by the presence of transverse framing. From geometry, the average cone radius that is seen by the inner plate is on the order of half the distance between transverse frames. Therefore, a good estimate for θ can be obtained by considering the triangular region limited by the cone radius seen by the inner plate and the transverse framing spacing, in the ratio of 1:2. In other words

$$\tan \theta_{optimum}^{inner\ plate} = \frac{1}{2} \quad \Rightarrow \quad \theta_{optimum}^{inner\ plate} = 26 \text{ deg} \tag{4.21}$$

4.3.2 Geometry of Steady State Inner Plate Cutting Force

Let us now introduce equation (4.21) into (4.20), therefore leaving the total inner plate steady state force as a function of δ only, which is a function of x by virtue of equation (4.7). Hence, the inner plate steady state cutting force becomes a function of x only.

4.3.3 Inner Plate Steady State Cutting Boundaries

The steady state inner plate cutting contribution begins at the point of rupture defined in equation (4.12). In addition, the final location after which the steady state force drops to zero is assumed to be the location of the cone axis when the cone is tangent to the inner plate trailing edge, i.e. station x_{12} in figure 2.5.

By considering the geometry of figure 2.5, we can expand the boundary points x_i^{ip} and x_f^{ip} as

$$\begin{aligned} x_i^{ip} &= x_r = 78.15 \quad inches \\ x_f^{ip} &= \left[l + d\tan(\alpha+\phi)\right]\cdot(\cos\alpha - \sin\alpha\tan\phi) = 151.14 \quad inches \end{aligned} \tag{4.22}$$

where all parameter values are taken from table A1.

4.4 Summary of Inner Plate Contribution to the Total Resisting Force

The contribution of the inner plate to the total resisting force is plotted in figure 4.5, where we can distinguish the following intervals:

$0 \le x \le 33.16 \quad inches$	No contribution
$33.16 \le x \le 78.15 \quad inches$	Inner Plate Cutting Initiation
$78.15 \le x \le 151.14 \quad inches$	Inner Plate Steady State Cutting
$151.14 \le x \le 170 \quad inches$	Contribution drops to zero

Table 4.1 : Summary of Inner Plate Contribution to the Total Resisting Force

In figure 4.5, we observe that the cutting initiation behavior is quasi-linear with respect to the coordinate x. The lack of perfect linearity is due to the $\frac{1}{\cos\alpha}$ factor in equation (4.3). Recall from equation (4.1) that the relation between β and the penetration δ involves a trigonometric transformation. Hence, even though δ is linear in x by virtue of equation (4.7), β is only quasi-linear. Therefore , we should expect the inner force contribution to be only quasi-linear, as is the case in figure 4.5. The steady state component, on the other hand, is perfectly linear in x, as in the case of the outer plate. An interesting feature of the plot in figure 4.5 is the force drop occurring at the rupture point. This is due to the sudden release of the transverse strength, and the transition from the initiation mode to the steady state mode.

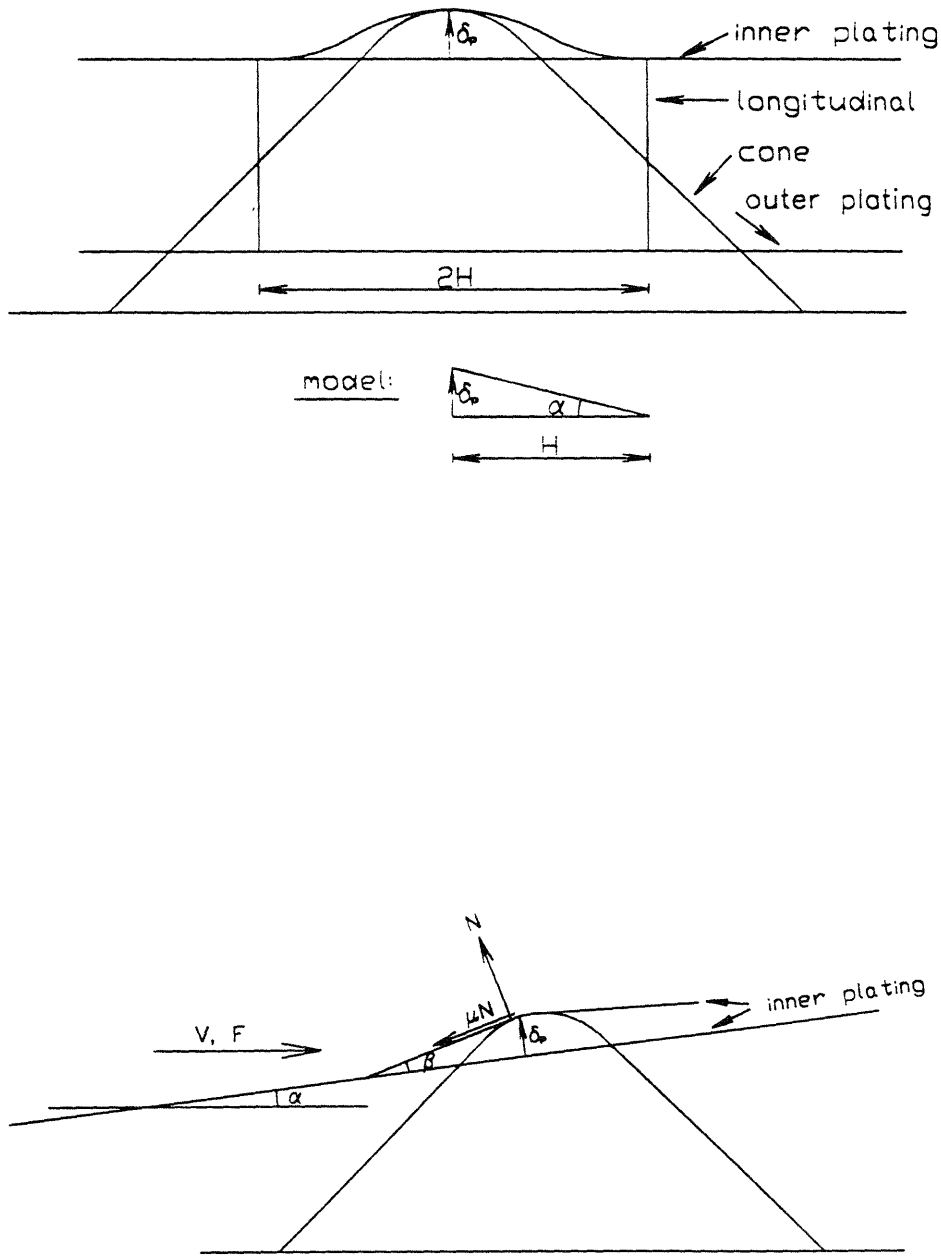

Figure 4.1. Inner Plate Cutting Initiation Geometry

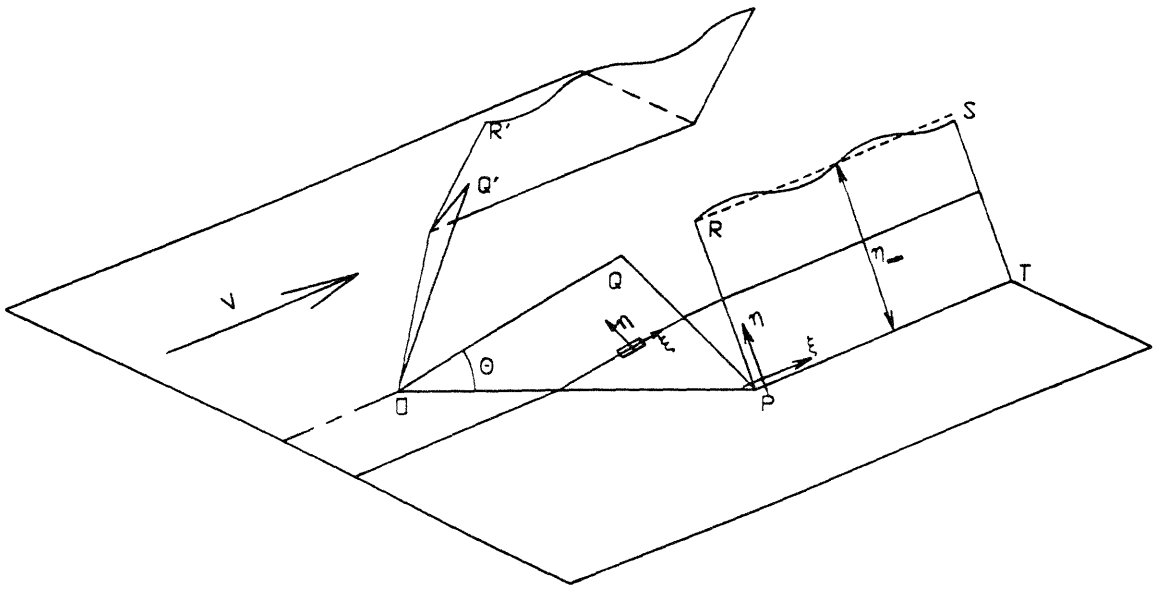

Figure 4.2. Straight Flaps Model Geometry

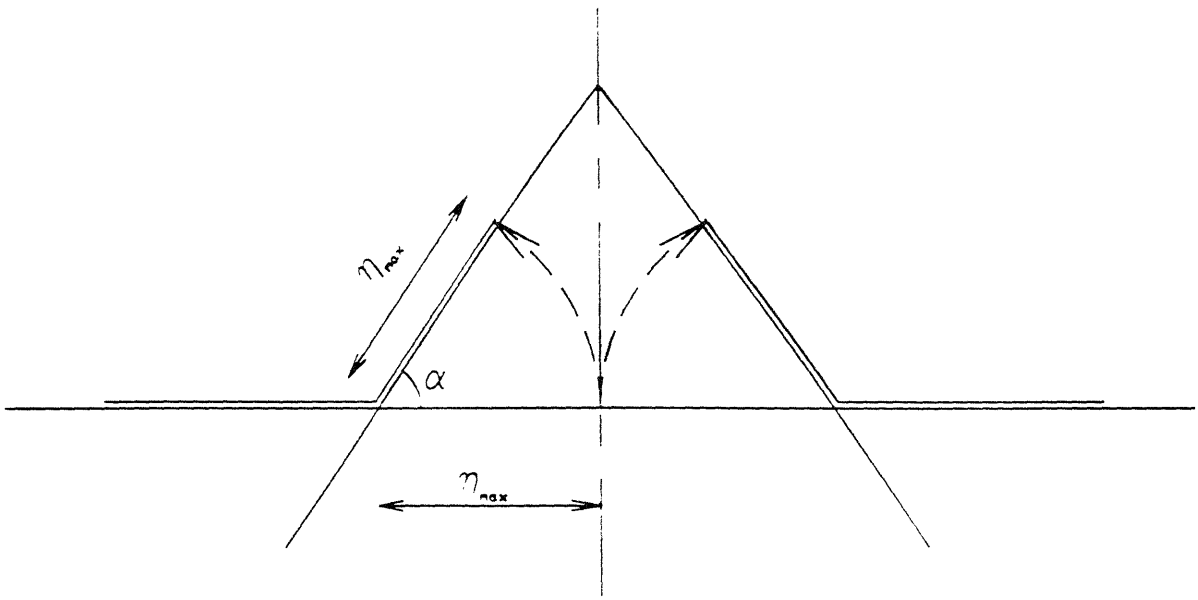

Figure 4.3. Side View of Cone-Inner Plate Interaction

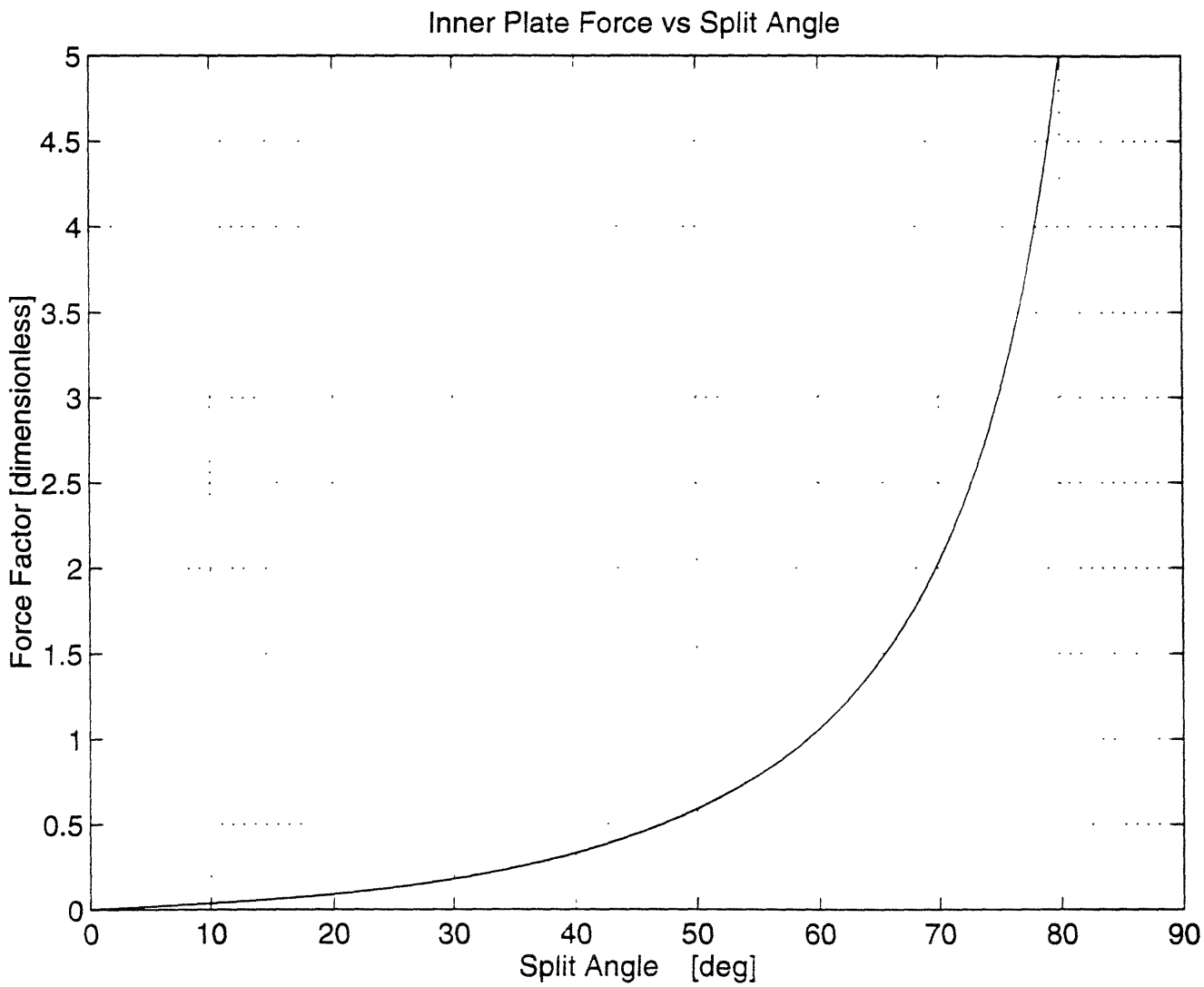

Figure 4.4. Inner Plate Steady State Force vs. Split Angle

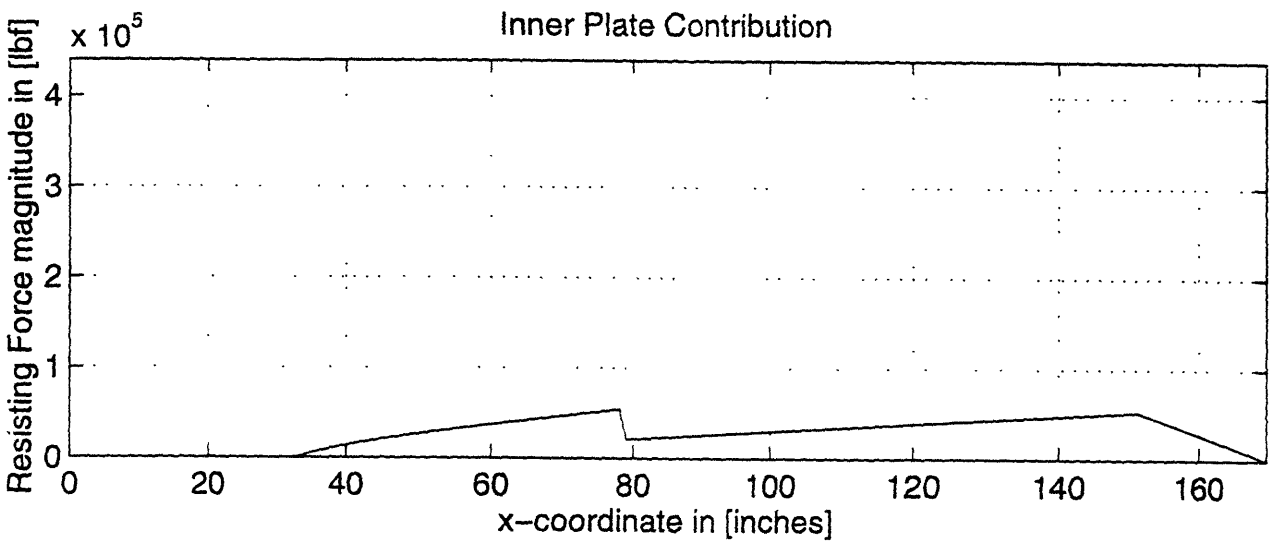

Figure 4.5. Theoretical Inner Plate Contribution to the Total Resisting Force

Chapter 5

Contribution of Transverse Frames to the Total Resisting Force

5.1 Introduction

The analysis of damage and fracture of transverse members, such as transverse frames and bulkheads, constitutes one of the most difficult task in grounding calculations. The main difficulty lies in treating the welded intersection between the shell plating and the transverse member. The fillet weld AB in figure 5.1, loaded by a conical rock, is subjected to a predominantly compressive load, so that no weld failure is expected to occur. By contrast, the upper weld CD, when loaded diagonally from below, would detach from the transverse member. contributing little to the strength of the structure. Therefore, the analysis focuses on the wedge cutting through the lower plate intersection AB.

As the rock advances along the bottom of the ship, the steady state plate cutting process is interrupted by transverse members. The crack, which propagates ahead of the wedge, is stopped and must be reinitiated on the other side of the transverse member. At the same time, a new crack forms in the transverse member which propagates upwards. According to Wierzbicki [7], the cutting process is divided into four stages.

1. *Phase 1*. The leading edge of the conical rock comes into contact with the weld (line AB in figure 5.1) causing the formation of a local dent. As the dent depth z increases, the tensile strains in the dent grow. Fracture along the main diagonal of the dent occurs when the strain reaches the critical rupture strain ε_c.

2. *Phase 2*. From this point on, a "diamond" shaped opening is formed, which increases in side as the wedge advances. Four cracks propagate at the four corners of the diamond with a velocity dictated by the shape of the rock, as shown in figure 5.2. This phase terminates when the speed of the crack equals the rock speed.

3. *Phase 3*. The opening continues to grow with the same speed as the velocity of the advancing rock. This phase terminates when the opening is large enough to clear the rock

4. *Phase 4*. If the height of the rock Δ is larger than that of the transverse member d. the process enters another phase in which the rock causes the weld line CD between the transverse member and the inner plate to deform and fracture.

The four phases of the transverse frame cutting process are shown in figure 5.3

5.2 Transverse Frame Cutting Force Governing Equation

In the model described in the introduction, it can be proven (Wierzbicki [7]) that, by and large, the main energy dissipation occurs in phase 3. Hence, the governing equation for the entire cutting process, without friction, may approximated by

$$F_{trans} = 6.14\, \sigma_0\, t^{1.5} x^{0.5} \tag{5.1}$$

The problem of establishing an appropriate friction correction factor has been studied by Pippenger [5] and Wierzbicki [7], who argue that a universal correction factor $Tot\ F_{trans} = 1.45\ F_{trans}$ can be applied to the entire process of cutting through transverse members. Therefore

$$Tot\ F_{trans} = 8.90\, \sigma_0\, t^{1.5} x^{0.5} \tag{5.2}$$

5.3 Transverse Frame Contribution Boundaries

The contribution of an individual transverse frame to the total resisting force is assumed to act over the length limited by the initial contact point between the cone and the frame and the axis of the cone. Thus, in figure 2.5, the contribution of frame #4 starts at x_7 and concludes at x_{t7}, for example. Similarly, the contributions of all remaining transverse frames are bounded in the same way, that is

Transverse Frame #1	$x_1 \le x \le x_{t1}$
Transverse Frame #2	$x_3 \le x \le x_{t3}$
Transverse Frame #3	$x_5 \le x \le x_{t5}$
Transverse Frame #4	$x_7 \le x \le x_{t7}$
Transverse Frame #5	$x_9 \le x \le x_{t9}$

The locations x_{2i+1} and $x_{t(2i+1)}$ for i=0,1,2,3 can be calculated from the geometry of figure 2.5. Thus, after substituting for the values of the constants from table A1, we obtain

$$
\begin{aligned}
x_{t0} &= \left[(d-e)\cos\alpha + r\left(\frac{1}{\sin\theta} - 1\right)\right]\tan\theta = 15.54 \quad inches \\
x_{t1} &= x_{t0} + c_2\cos\alpha = 43.30 \quad inches \\
x_{t3} &= x_{t1} + c_1\cos\alpha = 68.09 \quad inches \\
x_{t5} &= x_{t3} + c_1\cos\alpha = 92.88 \quad inches \\
x_{t7} &= x_{t5} + c_1\cos\alpha = 117.7 \quad inches \\
x_{t9} &= x_{t7} + c_2\cos\alpha = 145.4 \quad inches
\end{aligned}
\tag{5.3}
$$

and

$$
\begin{aligned}
x_1 &= c_2(\cos\alpha - \sin\alpha\,\tan\theta) = 24.16 \quad inches \\
x_3 &= (c_1 + c_2)\cdot(\cos\alpha - \sin\alpha\,\tan\theta) = 45.73 \quad inches \\
x_5 &= (2c_1 + c_2)\cdot(\cos\alpha - \sin\alpha\,\tan\theta) = 67.30 \quad inches \\
x_7 &= (3c_1 + c_2)\cdot(\cos\alpha - \sin\alpha\,\tan\theta) = 88.87 \quad inches \\
x_7 &= (3c_1 + 2c_2)\cdot(\cos\alpha - \sin\alpha\,\tan\theta) = 113.0 \quad inches
\end{aligned}
\tag{5.4}
$$

where all the relevant geometric parameters are defined in figure 2.5, and their values given in table A1.

5.4 Summary of Transverse Frame Contributions to the Total Resisting Force

The contribution of the transverse frames to the total resisting force is plotted in figure 5.4. Note that the contributions of various frames engage into each other and how this overlap produces several peak formations in the plot. Such peaks are not to be confused with actual features of the theoretically predicted force, but are simply caused by the overlap. In reality, NSWC experimental results showed that for every transverse frame the resisting force is characterized by a sudden initial outburst, or peak, followed by subsequent fluctuations of minor importance. Such an effect is clearly identifiable in figure 5.4. In general, the analytical model proposed here has been unable to reproduce the sudden peak formations of the experimental results. However, the energy-wise correlation between theory and experiments has been found to be quite satisfactory.

Table 5.1 summarizes the contribution of the four transverse webs and one transverse bulkhead to the total resisting force.

$24.16 \leq x \leq 43.30$ *inches*	Transverse Frame # 1
$45.73 \leq x \leq 68.09$ *inches*	Transverse Frame # 2
$67.30 \leq x \leq 92.88$ *inches*	Transverse Frame # 3
$88.87 \leq x \leq 117.7$ *inches*	Transverse Frame # 4
$113.0 \leq x \leq 145.4$ *inches*	Transverse Frame # 5

Table 5.1 : Summary of the Transverse Frame Contribution to the Total Resisting Force

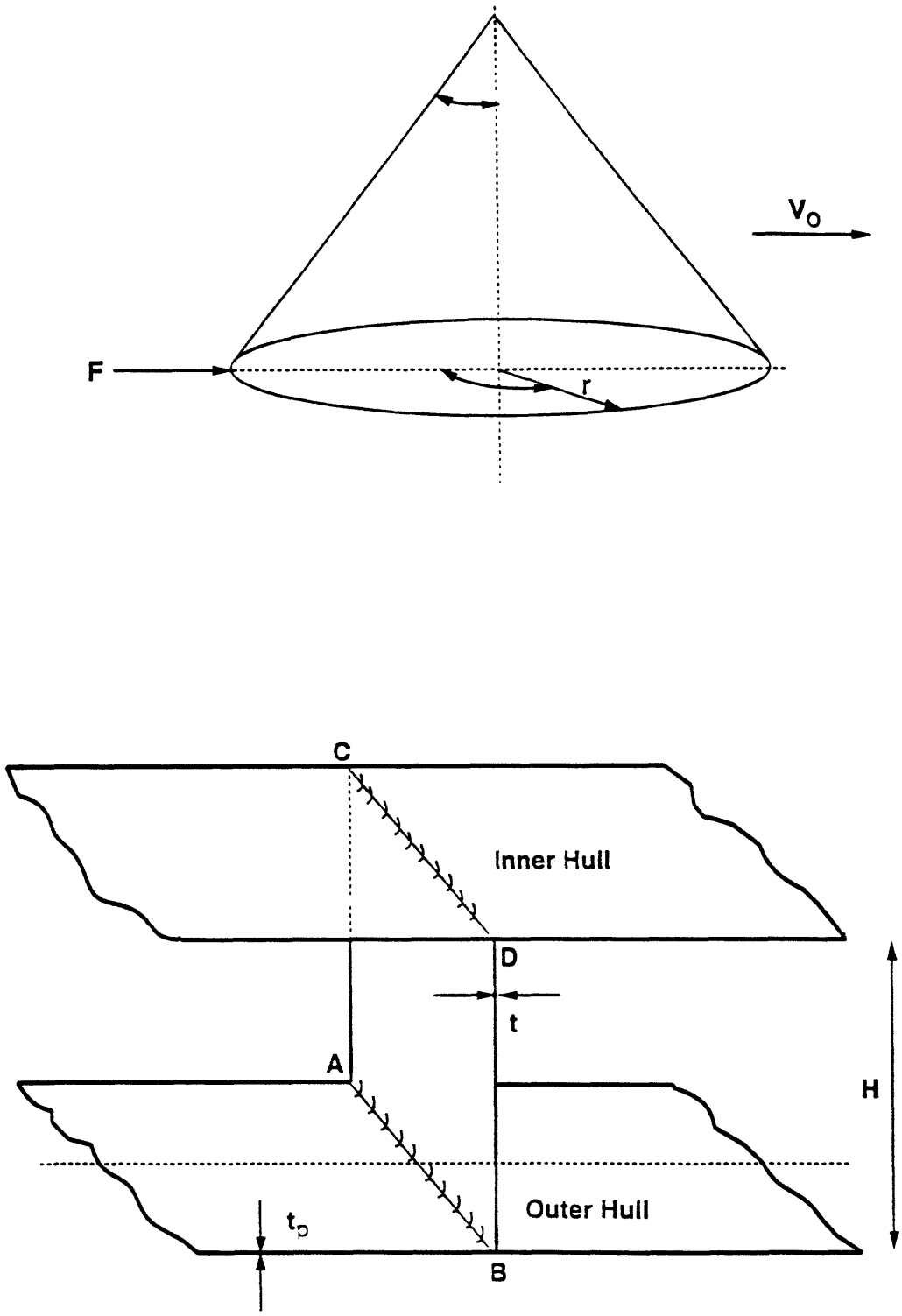

Figure 5.1. Transverse Frame Geometry

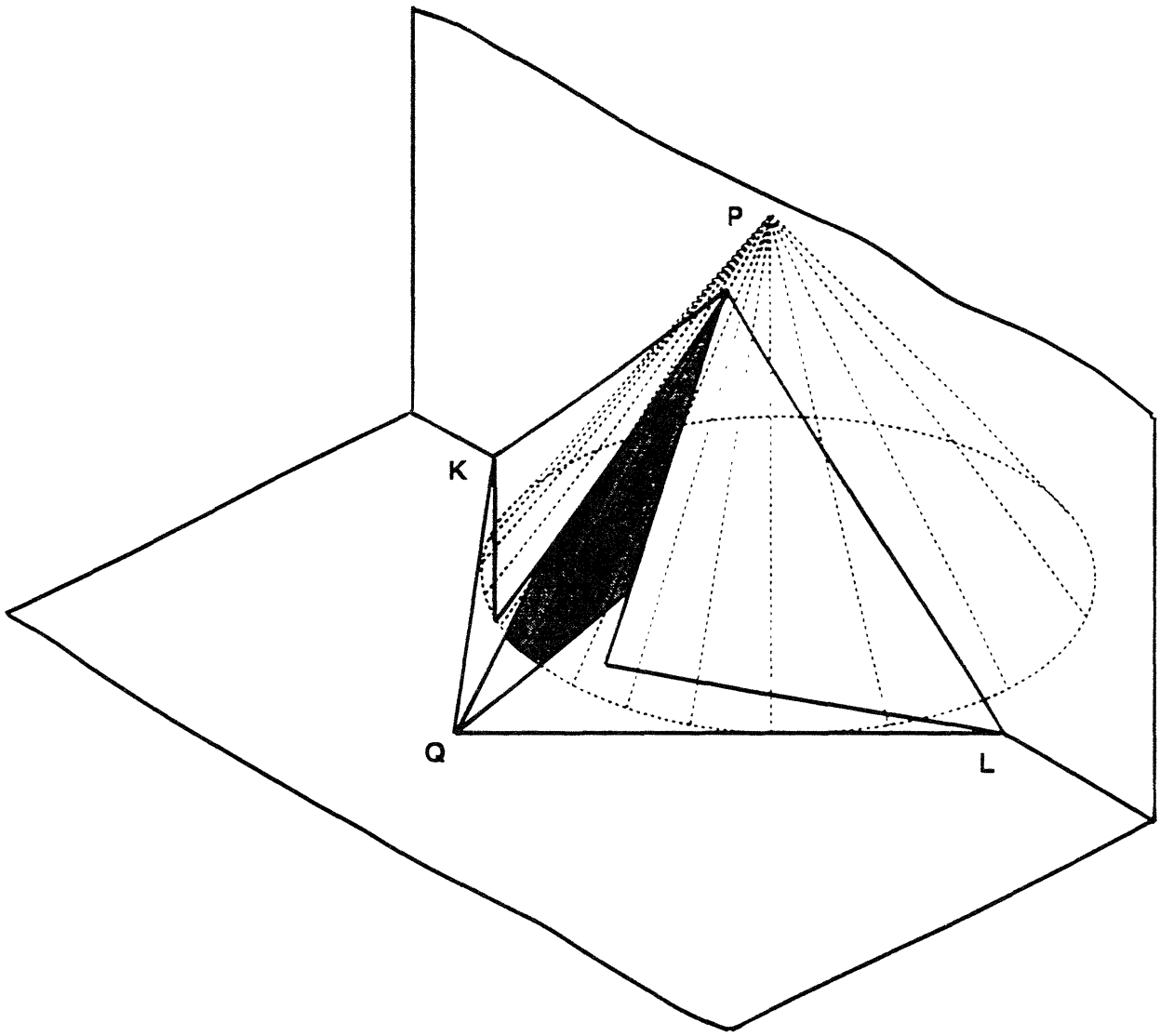

Figure 5.2. Diamond Shape Geometry in Transverse Frame Cutting

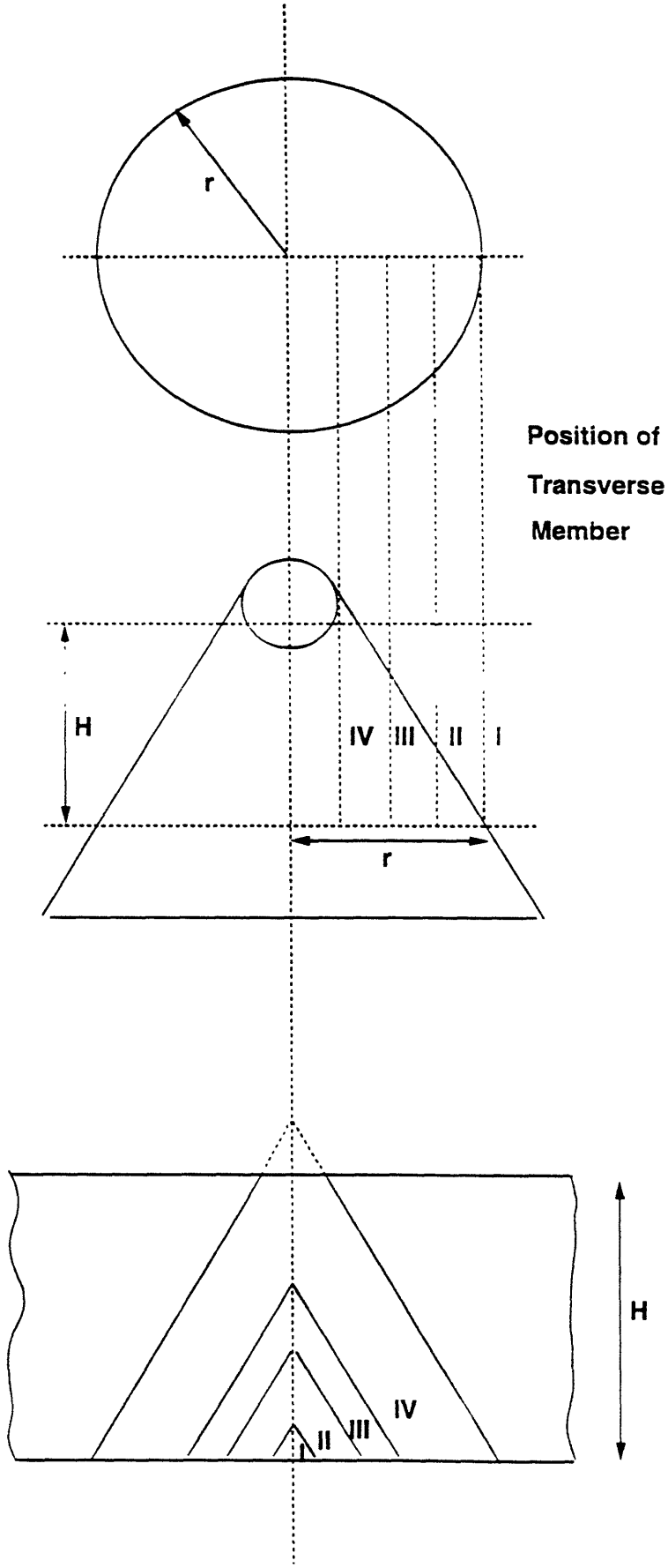

Figure 5.3. Phases of Transverse Frame Cutting

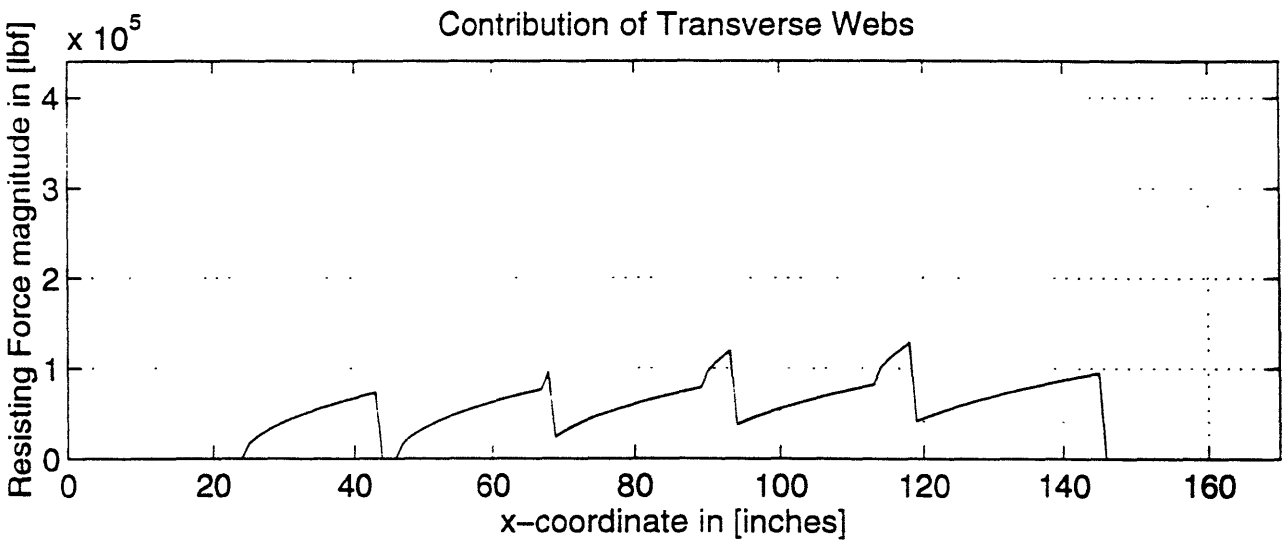

Figure 5.4. Theoretical Transverse Frame Contribution to the Total Resisting Force

Chapter 6

Contribution of Longitudinal Girders to the Total Resisting Force

6.1 Introduction

Experimental evidence gained from the NSWC Grounding Experiment, Rodd [1], and from real accidental groundings of ships [8] shows that longitudinal members are twisted, bent, stretched, crushed and tripped in the event of grounding. The response of the longitudinals depends on their scantlings, on how they are attached to the surrounding structure and, of course, on the nature of the load. In this chapter, we shall consider only longitudinals that are fixed between a lower and a upper bottom plating. Furthermore, the considered girders are assumed to be fixed at the upper edge, and to have relatively weak resistance against crushing in the lateral direction.

6.2 Derivation of Longitudinal Girder Crushing Force

6.2.1 Model Kinematics

The geometry of the proposed model for the longitudinal girders is shown in figure 6.1. The model assumes a deformation pattern compatible with the straight flaps model discussed in section 4.3.1.1. It is assumed that the upper edge of the longitudinal girders remains undeformed.

6.2.2 Energy Dissipation

Consider figure 6.1. Let η_L be the distance from the plate boundary to the longitudinal. The undeformed length of the lowest fiber in the longitudinal becomes

$$l(\eta_L) = \eta_L \cot\theta \tag{6.1}$$

where θ is the cone splitting angle of the outer plate, which was given in equation (3.35). The elongation of the fiber can be defined in a similar manner as in equation (4.18). Thus

$$u(\eta_L) = \eta_L \sqrt{(1-\cos\beta)^2 \sin^2\theta + (1-\cos\theta)^2 \sin^2\beta} \tag{6.2}$$

where β is defined in equation (4.1). With no strain reversal, the variation in axial strain for a material element in the lowest fiber of the longitudinal, as it passes through the transition zone, becomes

$$[\varepsilon_L] = \frac{u(\eta_L)}{l(\eta_L)} = \tan\theta \sqrt{(1-\cos\beta)^2 \sin^2\theta + (1-\cos\theta)^2 \sin^2\beta} \tag{6.3}$$

Moreover, it is necessary to consider the change in axial strain in the upward direction. As shown in figure 6.1, there is also a contribution to the stretching from the fact that the longitudinal web folds and parts of it are displaced out of their original plane. However, this effect is relatively small and can be neglected. Figure 6.2 shows a view in the transverse direction of the deformed longitudinal web. As indicated, it is assumed that only the fibers in that part of the web corresponding to the penetration δ are strained. The strain [ε] is assumed to decrease linearly from $[\varepsilon_L]$ to 0 over the penetration depth δ of the wedge, which by geometric compatibility is the same as the penetration of the cone into the inner plate. Let us define a vertical coordinate s, in the plane of the longitudinal web, as shown in figure 6.2. Then, we can write the strain variation in the s direction as

$$\varepsilon(s) = \begin{cases} [\varepsilon_L]\left(1-\dfrac{s}{\delta}\right) & , \quad s \le \delta_w \\ 0 & , \quad s > \delta_w \end{cases} \tag{6.4}$$

where δ_w is vertical motion of the longitudinal web, which is approximately equal to the penetration into the inner plate δ. Here again, as in the case of section 4.3.1, the shear strain is neglected. The statement for the steady state energy dissipation of the longitudinal girders can be expressed as in equation (4.16). Hence

$$F_{long} = 2\frac{2}{\sqrt{3}}\sigma_0 t\int_0^{\delta}[\varepsilon_L]\left(1-\frac{s}{\delta}\right)ds = \frac{2}{\sqrt{3}}\sigma_0 t[\varepsilon_L]\delta \tag{6.5}$$

where δ is the penetration of the cone into the inner plate. Substituting for the strain from equation (6.3) into (6.5) we obtain the plastic cutting force for the longitudinal girders as

$$F_{long} = \frac{2}{\sqrt{3}}\sigma_0 t\left[\tan\theta\sqrt{(1-\cos\beta)^2\sin^2\theta+(1-\cos\theta)^2\sin^2\beta}\right]\delta \tag{6.6}$$

6.2.3 Friction Contribution to the Longitudinal Girder Crushing Force

It is assumed that because the longitudinals follow the deformation of the outer plate, the friction correction factor shall be identical as for the outer plate. Thus substituting equation (3.33) into (6.6) we obtain the total longitudinal girder cutting force as

$$Tot\ F_{long} = F_{long}\frac{1}{1-\dfrac{\mu\cos\theta}{\cos\phi\sin\theta+\mu\cos\theta}} \tag{6.7}$$

6.2.4 Closed Form Solution for the Longitudinal Girder Crushing Force

In equation (6.7) are δ and θ; β is a function of δ via equation (4.1). As in the previous cases of the outer and inner plates, we will choose a θ that minimizes the total longitudinal cutting force. Therefore, for different values of δ we plot the total force versus θ, as shown in figure 6.3. However, as in the case of the inner plate, no minimum value is found. Hence, we are forced again to resort to geometric considerations to establish the splitting angle. Since the displacement pattern of the longitudinal girders is constrained by the outer plate, we can assume that the optimum split angle for the

longitudinal girders will conform to the optimum split angle for the outer plate, which was found in equation (3.37). Therefore,

$$\theta_{optimum}^{longitudinal} = 20 \quad \text{deg} \tag{6.8}$$

Finally, we introduce equation (6.8) into (6.7), and therefore we have expressed the total force as a function of δ, and hence of x via equation (4.7), only.

6.3 Longitudinal Girder Contribution Boundaries

In the present analysis, the contribution of both longitudinal girders to the total resisting force is assumed to begin at the location x_{t1}, i.e. the contact point between the cone and the first transverse frame as shown in figure 2.5. This assumption is based upon the absence of transverse framing before x_{t1}, so that the longitudinal girders are not supported before the first transverse, and hence they are free to deform without opposing much resistance. From equation (5.2) we recall that

$$x_i^{long} = x_{t1} = 43.30 \quad inches \tag{6.9}$$

Similarly, after the location x_{t9}, i.e. the contact point between the cone and the last transverse frame as shown in figure 2.5, it is assumed that the longitudinal girder contribution drops linearly to zero. From equation (5.2)

$$x_f^{long} = x_{t9} = 145.4 \quad inches \tag{6.10}$$

6.4 Summary of Longitudinal Girder Contribution to the Total Resisting Force

The contribution of the longitudinal girders to the total resisting force is plotted in figure 6.4. In the plot, we can identify the following intervals

$0 \leq x \leq 43.30 \quad inches$	Zero Contribution
$43.30 \leq x \leq 145.4 \quad inches$	Contribution increases linearly
$145.4 \leq x \leq 170 \quad inches$	Contribution drops linearly to zero

Table 6.1: Summary of Longitudinal Girder Contribution to the Total Resisting Force

If we compare figure 6.4 to 5.4, 4.5 and 3.7, we can observe that the contribution of the longitudinal girders is by far the less significant of all of the structural members so far considered. Such a result is consistent with Choi's correlation of NSWC experimental results and Minorsky/Vaughn theory, [2].

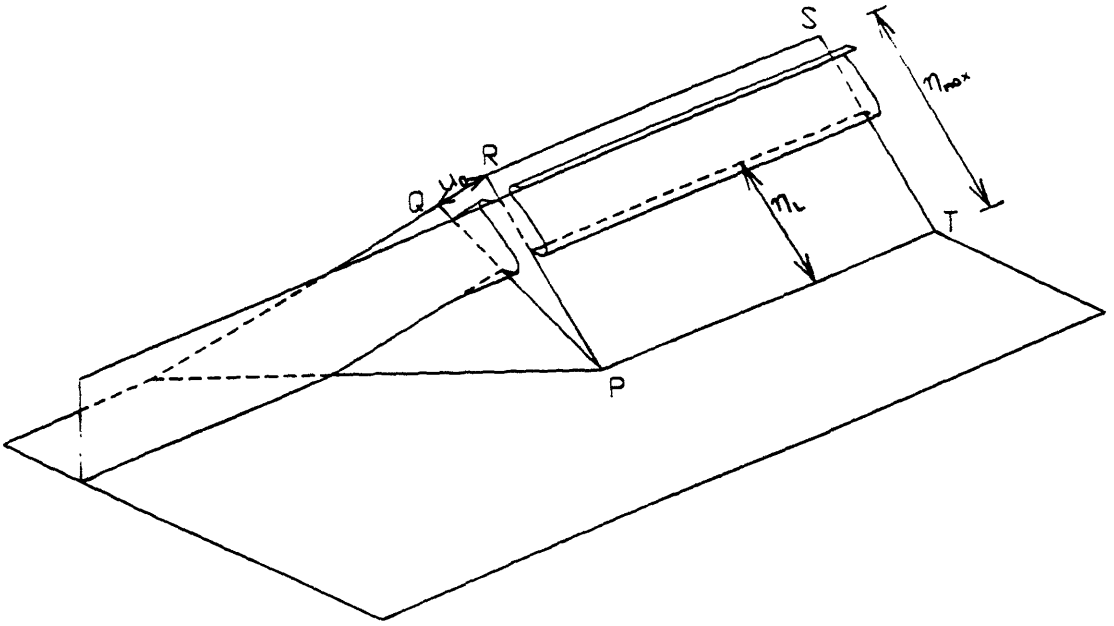

Figure 6.1. Longitudinal Girder Deformation Geometry

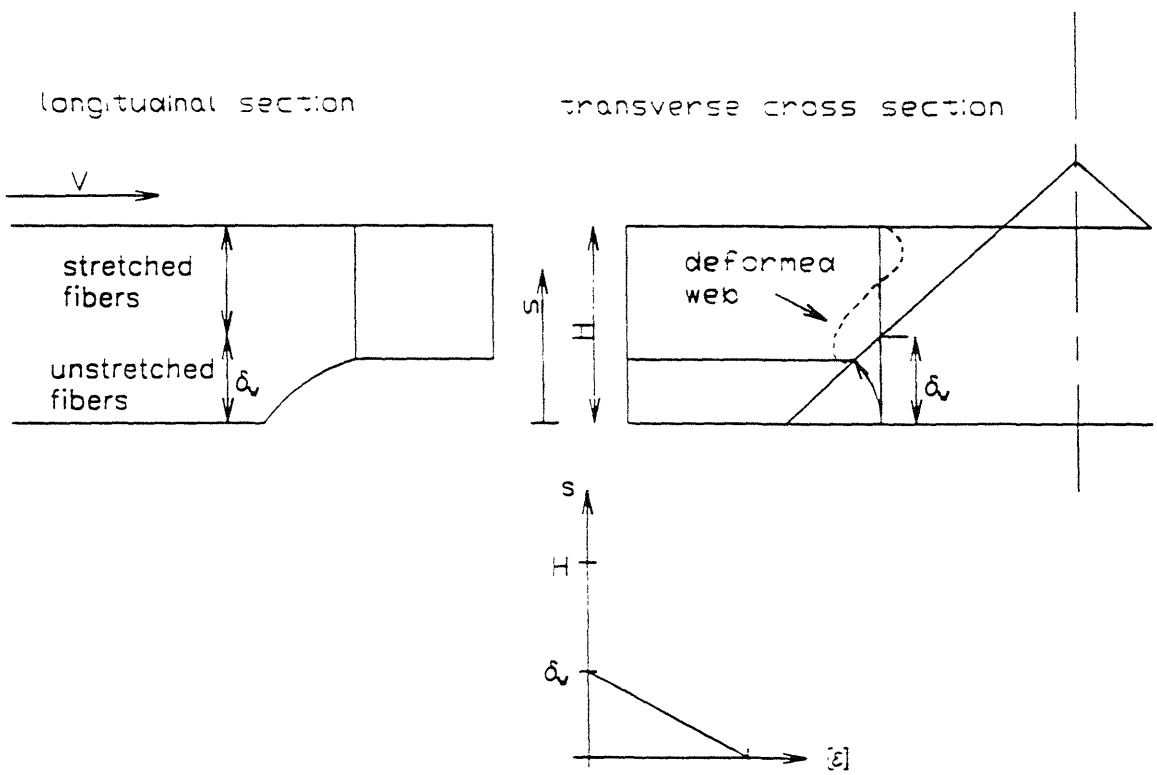

Figure 6.2. Side View of Longitudinal Girder Deformation Geometry

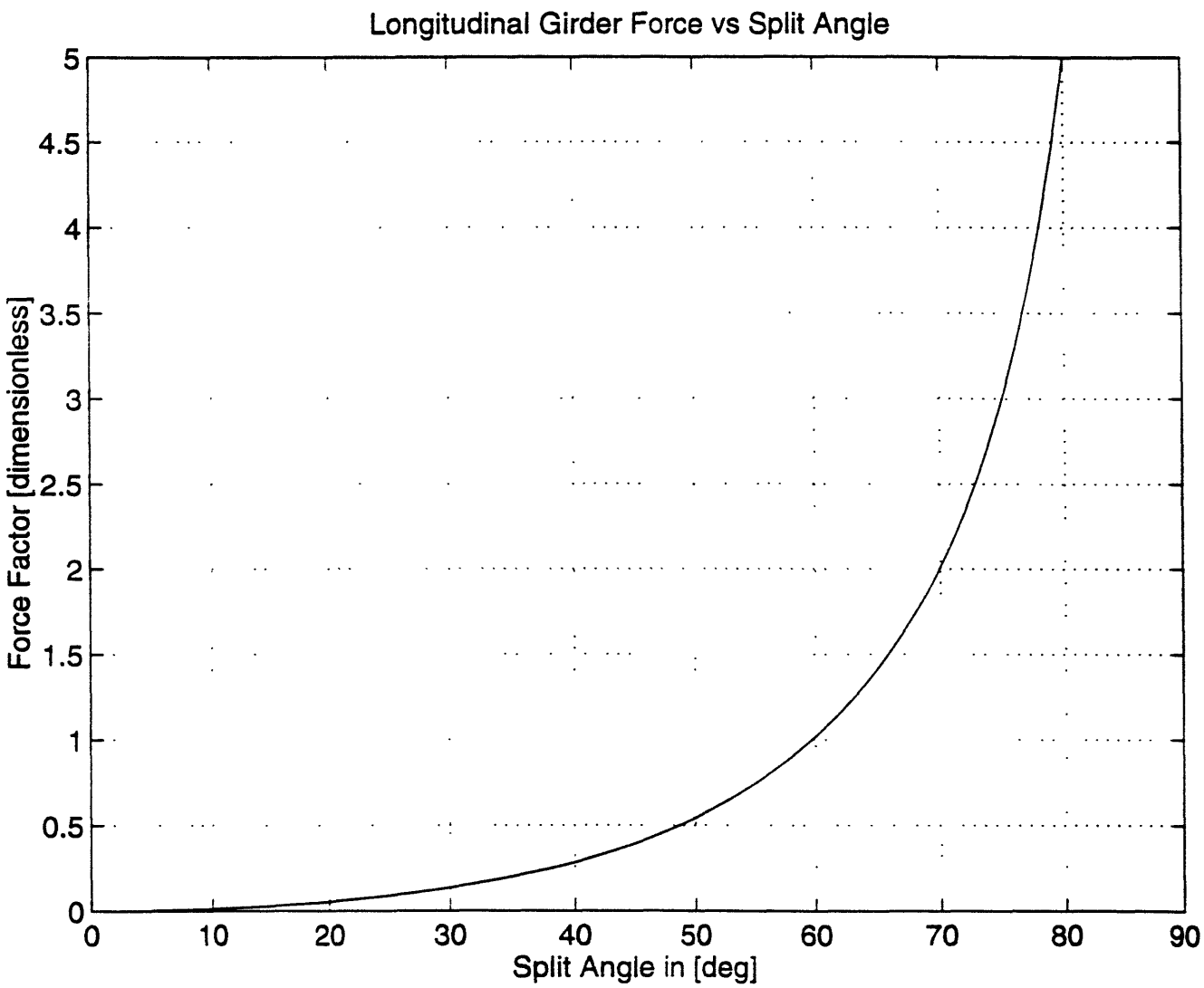

Figure 6.3. Longitudinal Girder Force vs. Split Angle

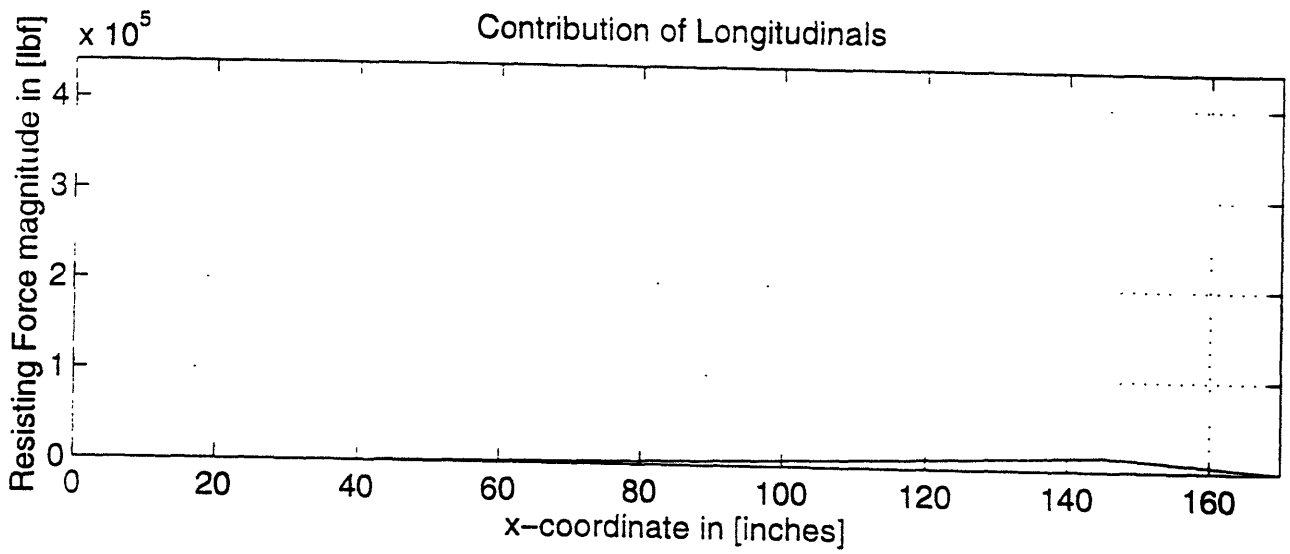

Figure 6.4. Theoretical Longitudinal Girder Contribution to the Total Resisting Force

Chapter 7

Conclusion

7.1 Comparison of MIT Theory with NSWC Grounding Test

So far in this thesis, we have investigated the individual contributions to the total resisting force of the four main structural elements present in the NSWC structural model, i.e. the outer and inner plates, transverse frames and longitudinal girders. According to the principle of the Superelement approach, as outlined in the introduction, we can now add up those contributions and obtain the overall response of the entire structure. Hence, the contributions shown in figures 3.7, 4.5, 5.4 and 6.4 are assembled together, and the result is displayed in figure 7.1, where both the experimental curve and the Minorsky/Vaughn prediction curve [2] are also reproduced. The following observations can be made from figure 7.1:

1. With respect to the total energy dissipated via the grounding force induced damage, i.e. the areas under the curves in figure 7.1, we can conclude that whereas the Minorsky/Vaughn method overpredicts the total energy by 35 %, the MIT theory underpredicts it by less than 3 %.

2. Because of its purely linear behavior, the Minorsky/Vaughn method is unable to reveal the different failure modes corresponding to different structural elements. However, the MIT theoretical prediction readily reveals the different contributions of the structural elements, and hence their relative importance in the occurrence of damage.

3. With respect to its ability to reproduce actual experimental features, e.g., the sudden force peaks occurring when the cone first comes into contact with the transverse

frames, the Minorsky/Vaughn method cannot compete with the new MIT theory. The MIT theoretical curve follows quite accurately the trend of the NSWC experimental curve, whereas the Minorsky/Vaughn curve constitutes merely a diverging linear upper bound to the actual force.

4. The MIT predicted outer plate cutting initiation solution described in section 3.2, which corresponds to the interval from 0 to about 20 inches in figure 7.1, underestimates the initiation force by half, and should therefore be improved in future analysis. However, because of the fact that the outer plate cutting initiation contributes such a small part to the total damage, this deficiency of the MIT theory is negligible when considering the total structural damage.

5. The MIT proposed solution for the transverse frame contributions, although very accurate in predicting the energy dissipated at each transverse frame, is unable to capture the sudden outburst of force that marks the beginning of each transverse frame contribution in the experimental curve.

6. The MIT theoretical average force increases as function of x at a higher rate than the experimental curve, that is, whereas in the fore structure the MIT theory underpredicts the experimental force, in the aft structure the MIT theory slightly overpredicts the force. In the NSWC experiment, it was noted by Rodd [1] that as the cone penetrated the model it caused the structure ahead of it to shrink transversely to the motion of the cone. This effect was attributed to the lack of adequate boundary support in the NSWC model assembly. The immediate consequence of this effect would be to artificially decrease the force in the trailing zone of the structure. Hence, it should be expected of the MIT theory to overestimate the force towards the trailing end of the structure, as is indeed the case in figure 7.1.

7. From figures 3.7, 4.5, 5.4 and 6.4, we conclude that the outer plate contributes 50 % to the total energy dissipated, the transverse frames 25 %, the inner plate 20 %, and the longitudinal girders 5 %. In this respect, the MIT theory agrees with the energy ratios of the structural elements in the Minorsky/Vaughn method calculated by Choi [2].

7.2 Recommendations for future Work

Overall, the new MIT theoretical prediction of damage shown in figure 7.1 represents a significant improvement over the Minorsky/Vaughn method. However, the implementation process of the MIT theory to the NSWC grounding scenario has revealed a number of limitations in the theory which should be revised in future work. The principal limitations of the theory are:

1. The outer plate cutting initiation solution, which underestimates the experimental contribution by 50 %, must be improved. As expressed in item 4 of section 7.1, this is a rather secondary consideration.

2. The transverse frame cutting solution should be modified to capture the sudden peak outburst of force at the initial contact between the cone and the corresponding frame. This is rather inconsequential when considering the energy dissipated, as was shown in item 5 of section 7.1.

3. By and large, the main limitation of the MIT theory arises from the high dependency of the steady state cutting force solutions developed for the outer and inner plates on the unknown split angle θ. Indeed, as the parametric studies shown in figures 3.2, 3.6, 4.4 and 6.3 reveal, the magnitude of the cutting force is very sensitive to θ. On the other hand, it is virtually impossible to obtain a unique θ from geometric considerations alone. Furthermore, when attempting to select θ on the basis of a minimum force criterion, the obtained angle for the case of the outer plate (the main energy dissipater) is unrealistically small. Hence, a certain amount of engineering judgment is necessary to define the free parameter θ. The difficulty of establishing an appropriate θ is inherent in the definition of both the curved and straight flaps models described in sections 3.3.3 and 4.3.3. Both models assumed that cone is in contact with the plates at two locations only, as shown in figure 3.1. In reality, the plate material wraps around the cone as the cutting process evolves. Therefore θ is purely an exercise of abstraction, a kind of equivalent linear interpolation to the actual wrapping geometry.

Hence, θ cannot be predicted from experimental observations. Because of the impossibility of unequivocally defining the split angle θ, much caution is necessary when implementing these models.

7.3 Final Remarks

The comparison of the MIT theory vis a vis with the Minorsky/Vaughn method, with respect to NSWC grounding experimental results described in section 7.1, shows that the performance of the MIT theory is superior. A further additional advantage of the MIT element approach is based on the enormous geometric complexity of displaced volume and fracture area calculations necessary for the Minorsky/Vaughn method, with respect to the much computationally simpler geometry of the MIT theory. This advantage of the MIT theory is readily shown by comparing the simplicity of the source code included in the appendix of this thesis document with the one used by Choi [2] in his correlation of the Minorsky/Vaughn method with NSWC Grounding Test.

Finally, I conclude in hope that this thesis work has proved the power and simplicity of the Superelement approach to complex structural problems, such as grounding of ships against conical rocks.

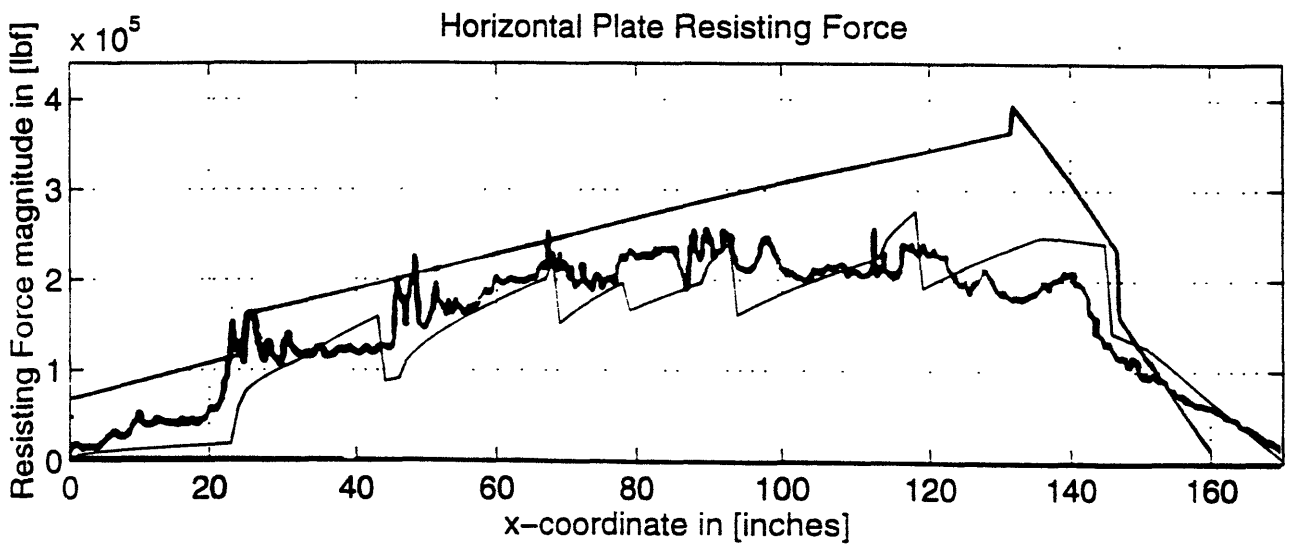

Figure 7.1. Comparison of MIT Theory with NSWC Experimental Results

References

[1] Rodd, J.L. 1994. "Double Hull Tanker Grounding Experiment." *Advanced (Unidirectional) Double Hull Technical Symposium Proceedings*, Gaithersbrug, Maryland.

[2] Choi, S. and T. Wierzbicki. 1995. *Correlation of NSWC Grounding Tests with Minorsky/Vaughn Method.* Technical Report No. 39, Joint MIT-Industry Program in Tanker Safety.

[3] Wierzbicki, T. and P.F. Thomas. 1993. "Closed Form Solution for Wedge Cutting Force through Thin Metal Sheets." *International Journal of Mechanical Science* 35:209-229.

[4] Zheng, Z. and T. Wierzbicki. 1995. *Steady-State Wedge Indentation: Improved Theory and Validation.* Technical Report No. 42, Joint MIT-Industry Program in Tanker Safety.

[5] Pippenger, D. *Coupled Vertical and Horizontal Resistance of Hull Girder in Grounding Accidents.* Masters Thesis, Department of Ocean Engineering, MIT, May 1995.

[6] Simonsen, B. Private Communications, March-May 1995.

[7] Wierzbicki, T. Private Communications, January-May 1995.

[8] Card, J.C. 1975. "Effectiveness of Double Bottoms in Preventing Oil Outflow from Tanker Bottom Damage Incidents." *Marine Technology* 12: 60-64.

[9] Wierzbicki, T. 1993. *Concertina Tearing of Metal Plates: Improved Solution and Comparison with Experiments.* Technical Report No. 22, Joint MIT-Industry Program in Tanker Safety.

[10] Choi, S., T. Wierzbicki and J. Culbertson-Driscoll. 1994. *Crushing Strength of Web Girders*. Technical Report No. 23, Joint MIT-Industry Program in Tanker Safety.

[11] Abramowicz, W. and T. Wierzbicki. 1989. "Axial Crushing of Multicorner Sheet Metal Columns." *Journal of Applied Mechanics* 56:113.

[12] Little, P. 1994. *Failure of Transverse Frames and Bulkheads in Grounding*. Technical Report No. 31, Joint MIT-Industry Program in Tanker Safety.

[13] Minorsky, V. 1959. "An Analysis of Ship Collisions with Reference to Protection of Nuclear Power Plants." *Journal of Ship Research* 3:1-4.

[14] Vaughn, H. 1977. "Damage to Ships due to Collision and Grounding." Det norske Veritas, DnV 77-345.

[15] Vaughn, H. 1978. "Bending and Tearing of Plate with Application to Ship-Bottom Damage." *The Naval Architect* May: 97-99.

[16] Vaughn, H. 1980. "The Tearing Strength of Mild Steel Plate." *Journal of Ship Research* 24: 96-100.

[17] Zheng, Z. *Theoretical Analyses of Wedge Cutting through Metal Plates*. Ph.D. Thesis, Department of Ocean Engineering, MIT, 1994.

APPENDIX

Table of Contents:

I. Table A1

II. Source Code for Calculations

A.1 Table of Numerical Values

Parameter	Description	Value & Units
α	Angle of attack	7.4 [deg.]
ϕ	Cone angle	45 [deg.]
Δ	Height of cone	38.9 [in.]
Δ_1	Height of conical rock	36.0 [in.]
r	Dome radius	7.0 [in.]
e	Dome tip-outer plate leading edge distance	2.0 [in.]
c_1	Transverse frame spacing	25.0 [in.]
c_2	Outer plate leding edge-transverse frame distance	28.0 [in.]
l	Overall length of model	156.0 [in.]
d	Double hull width	14.75 [in.]
t	Plate thickness	0.119 [in.]
σ_0	Flow stress	46 [ksi]
μ	Coefficient of friction	0.3

Table A1. Numerical Values of the Main Geometric and Material Parameters

```
%%%%%%%%%%%%%%%%%%%%%%%%%%%%%%%%%%%%%%%%%%%%%%%%%%%%%
%                                                   %
%               I N P U T   F I L E                 %
%                                                   %
%%%%%%%%%%%%%%%%%%%%%%%%%%%%%%%%%%%%%%%%%%%%%%%%%%%%%
%
%
%   Units are in [inches] and [psi]
%      NOTE sigma= 46 ksi
%
%%%%% Cosntants &  parameters %%%%%
%
t=0.119;
sig=46000;
nu=0.3;
phi=pi/4;
%
%
%%%%%%% OUTER PLATE %%%%%%%
%
%
%% INITIATION PHASE
%
y1=0:1:23;
y2=24:1:170;
zeta=20*pi/180;
fri_out_ini=1/(1-(nu*cos(zeta))/(cos(phi)*sin(zeta)+nu*cos(zeta)));
Fop_ini=[4/3*sig*t^(1.5)*(sin(zeta))^(1/2)/(cos(zeta))*(fri_out_ini)*y1.^(1/2) 0*y2
%
%
%% STEADY STATE PHASE
%
%
zeta=20*pi/180;
x1=0:1:23;
x2=24:1:135;
x3=136:1:170;
hop=[0.00000001*x1 13.525+.13*x2 0.00000001*x3];
%
%  Calculating Rop
%
a=2/(cos(phi)*cos(zeta));
b=1.16*zeta*sin(zeta)*cos(zeta/2)/(cos(zeta)*(cot(phi)^2));
c=1.27*cos(zeta)*(1+0.55*zeta^2);
d=1.16*zeta*sin(zeta)*cos(zeta/2)/cos(zeta)*(cos(phi)-tan(phi)*(1-sin(phi)))^2;
Rop=((a*t*hop+b*hop.^2)/(c+d)).^(1/2);
%
%  Calculating Bop
%
Bop=1/cot(phi)*(hop-(1-sin(phi))*Rop);
%
%  Friction Factor
%
fri_out_ss=1/(1-(nu*cos(zeta))/(cos(phi)*sin(zeta)+nu*cos(zeta)));
%
%  Calculating Cutting Force
%
bending=2*(Bop+Rop*cos(phi))/(Rop*cos(zeta));
tip=c/t*Rop;
transition=b*(cot(phi))^2*(Rop*cos(phi)+Bop).^2./(Rop*t);
Fop=2/3^(1/2)*sig*t^2/4*(bending+tip+transition)*fri_out_ss;
%
Fop_inter=[0*x1 0*x2 Fop(136)-Fop(136)/(170-135)*(x3-135)];
%
%
%%%%%%%%%%% INNER PLATE %%%%%%%%%%%%%%
```

```
%
%
%  INNER PLATE INITIATION
%
x4=0:1:32;
x5=33:1:78;
x6=79:1:151;
x7=152:1:170;
hip=[0.00000001*x4 -4.25+.13*x5 0.0000001*x6 0.00000001*x7];
%
attack=7.4*pi/180;
angulo=atan(hip/14.75);
coeficiente=1./(1-(0.3./(cos(attack)*(sin(angulo+attack)+0.3*cos(angulo+attack)))))
Fip_ini=(sig*t)/(cos (attack))*hip.*coeficiente;
%
%  INNER PLATE STEADY STATE
%
hip=[0.00000001*x4 0.000000001*x5 -4.25+.13*x6 0.00000001*x7];
HIP=[0.00000001*x4 0.000000001*x5 x6./x6 0.0000000001*x7];
angulo=45*pi/180*HIP;
zeta=26*pi/180;
raiz=((1-cos(angulo)).^2*(sin(zeta))^2+(1-cos(zeta))^2*(sin(angulo)).^2).^(1/2);
fri_in_ss=1/(1-(nu*cos(zeta))/(cos(phi)*sin(zeta)+nu*cos(zeta)));
Fip=4/3^(1/2)*sig*t*hip/cos(phi)*((tan(zeta))^2+1/4)^(1/2).*raiz*fri_in_ss;
%
Fip_inter=[0*x4 0*x5 0*x6 Fip(152)-Fip(152)/(170-151)*(x7-151)];
%
%%%%%%% TRANSVERSE WEBS %%%%%%%%%
%
%
x10=0:1:23;
x11=24:1:43;
x12=44:1:170;
xweb1=[x10 x11 x12];
%
x13=0:1:45;
x14=46:1:68;
x15=69:1:170;
xweb2=[x13 x14 x15];
%
x16=0:1:66;
x17=67:1:93;
x18=94:1:170;
xweb3=[x16 x17 x18];
%
x19=0:1:88;
x20=89:1:118;
x21=119:1:170;
xweb4=[x19 x20 x21];
%
x22=0:1:112;
x23=113:1:145;
x24=146:1:170;
xweb5=[x22 x23 x24];
%
%
Fweb1=[0*x10 8.90*sig*t^(1.5)*(x11-24).^(1/2) 0*x12];
Fweb2=[0*x13 8.90*sig*t^(1.5)*(x14-46).^(1/2) 0*x15];
Fweb3=[0*x16 8.90*sig*t^(1.5)*(x17-67).^(1/2) 0*x18];
Fweb4=[0*x19 8.90*sig*t^(1.5)*(x20-89).^(1/2) 0*x21];
Fweb5=[0*x22 8.90*sig*t^(1.5)*(x23-113).^(1/2) 0*x24];
%
Fweb_tot=Fweb1+Fweb2+Fweb3+Fweb4+Fweb5;
%
%
%%%%%%%% LONGITUDINALS %%%%%%%
```

```
%
x25=0:1:42;
x26=43:1:145;
x27=146:1:170;
%
zeta=20*pi/180;
fri_long=1/(1-(nu*cos(zeta))/(cos(phi)*sin(zeta)+nu*cos(zeta)));
height_cone=36.0;
y_inner_plate=25.375-tan(7.4*pi/180)*x26;
delta=height_cone-y_inner_plate;
hlo=[0.000000001*x25 -4.25+.13*x26 0.00000001*x27];
angulo=atan(hlo/14.75);
%HLO=[0*x25 x26./x26 0*x27];
%angulo=45*pi/180*HLO;
raiz=((1-cos(angulo)).^2*(sin(zeta))^2+(1-cos(zeta))^2*(sin(angulo)).^2).^(1/2);
F_long=2/3^(1/2)*sig*t*raiz*tan(zeta).*[0*x25 delta 0*x27]*fri_long;
F_long_inter=[0*x25 0*x26 F_long(146)-F_long(146)/(170-145)*(x27-145)];
%F_long_inter=0*[x25 x26 x27];
%
%  PLOTTING
%
x=0:1:170;
Ftot=Fop_ini+Fop+Fop_inter+Fip_ini+Fip+Fip_inter+Fweb_tot+F_long+F_long_inter;
%subplot(211)
%plot(x,Ftot)
%axis([0 170 0 4.4e5])
%%xlabel('x-coordinate in [inches]');
%ylabel('Resisting Force magnitude in [lbf]')
%title('Horizontal Plate Resisting Force ')
%
%subplot(212)
%plot(x,Fop+Fop_ini+Fop_inter)
%axis([0 170 0 4.4e5])
%xlabel('x-coordinate in [inches]');
%ylabel('Resisting Force magnitude in [lbf]')
%title('Outer Plate Contribution')
%
%subplot(211)
%plot(x,Fip+Fip_ini+Fip_inter)
%axis([0 170 0 4.4e5])
%xlabel('x-coordinate in [inches]');
%ylabel('Resisting Force magnitude in [lbf]')
%title('Inner Plate Contribution')
%
%subplot(212)
%plot(x,Fweb_tot)
%axis([0 170 0 4.4e5])
%xlabel('x-coordinate in [inches]');
%ylabel('Resisting Force magnitude in [lbf]')
%title('Contribution of Transverse Webs')
%
subplot(212)
plot(x,F_long+F_long_inter)
axis([0 170 0 4.4e5])
xlabel('x-coordinate in [inches]');
ylabel('Resisting Force magnitude in [lbf]')
title('Contribution of Longitudinals')
```